



CoFe₂O₄@Ti₃C₂ MXene nanocomposite-based broad-spectrum degradation of biotoxins

Xuwen Chen^a, J. Brett Sallach^b, Wanting Ling^a, Xuqiang Zhao^a, Thomas Borch^{c,d}, Yanzheng Gao^{a,*}

^a Institute of Organic Contaminant Control and Soil Remediation, College of Resources and Environmental Sciences, Nanjing Agricultural University, Nanjing 210095, China

^b Department of Environment and Geography, University of York, Heslington YO10 5NG, United Kingdom

^c Department of Soil and Crop Sciences, Colorado State University, Fort Collins, CO 80523, United States

^d Department of Chemistry, Colorado State University, Fort Collins, CO 80523, United States

ARTICLE INFO

Keywords:

CoFe₂O₄@Ti₃C₂ MXene nanocomposite

Biotoxins

Hydrothermal synthesis

Broad-spectrum degradation

Persulfate

ABSTRACT

A significant research priority is developing a treatment method to effectively remove biotoxins commonly found in food production and the environment. A novel CoFe₂O₄@Ti₃C₂ MXene nanocomposite was fabricated by growing ferrite on MXene, and used nanocomposite to develop an oxidation-based treatment system with persulfate (PS). The ability of this system to broad-spectrum degrade mycotoxins and plant toxins was evaluated, and the catalytic and oxidation mechanisms were characterized. Co and Fe sites provide activation efficiency towards PS with adsorption energies of −21.15 and −19.63 eV, Ti site promote activation by inducing the reduction of Co and Fe. The production of reactive oxygen species via electron transfer contributed to the degradation of fourteen biotoxins with removal rates above 88%, and the frontier molecular orbital energy explained the difference in degradation extent. Electron-rich sites were predicted to help explain the degradation mechanism. The products were harmless to the ecology and human. The observations clearly indicate that Ferrite-MXene nanocomposites are viable options for broad-spectrum degradation of a wide variety of biotoxins.

1. Introduction

Biotoxins are a global problem since they can affect crop production, and result in economic losses for farmers and food producers. Mycotoxins are usually produced in filamentous fungi of the genera *Aspergillus*, as well as *Penicillium* [1], and including ochratoxins (OTs, which contain ochratoxin A (OTA), ochratoxin B (OTB), ochratoxin C (OTC) [2]), aflatoxins (AFs, which contain aflatoxin B₁ (AFB₁), aflatoxin B₂ (AFB₂), aflatoxin G₁ (AFG₁), aflatoxin G₂ (AFG₂), aflatoxin M₁ (AFM₁), aflatoxin M₂ (AFM₂)), gliotoxin (GT) and deoxynivalenol (DON). Those mycotoxins are widely present in soil, air, dust, plants, animals, grains and various nuts [3,4]. Beauvericin (BEAU) is derived from *Fusarium oxysporum* and *Beauveria bassiana* and commonly used as a pesticide. Podophyllotoxin (POD) and xanthotoxin (XAT) are plant toxins derived from huapodophyllum, zanthoxylum bungeanum, and star anise, respectively.

The pollution of biotoxins in the environment and the harm to the

human body and the ecology have been concerned. Mycotoxins have been reported to contaminate about 25% of the world's grain production on an annual basis [5]. The European Commission stipulates a maximum of 3.0 µg kg^{−1} OTA in cereals and 2.0 µg kg^{−1} OTA in grape juice [6]. AFB₁ is up to 10 times more toxic than potassium cyanide and 68 times more toxic than arsenic. The EU stipulates that 2 µg kg^{−1} as a limited dose of AFB₁ in foods for direct human consumption [7,8], and food containing 1 mg kg^{−1} or higher AF is suspected to cause aflatoxin poisoning [9]. Moreover, OTs and AFs have all demonstrated carcinogenic, nephrotoxic, teratogenic, mutagenic, cardiotoxic, neurotoxic and hepatotoxic effects [10–12]. GT is an immunosuppressive with demonstrated pro-apoptosis on human and some mammalian cells [13]. DON is a water-soluble biotoxin that is harmful to the environment, which can accumulate in the body. The toxic effects of DON include cytotoxicity, and immunotoxicity [14]. Recent research has focused on the detection of biotoxins and their toxicity to organisms. The frequent occurrence and harmful effects of biotoxins make it urgent to develop effective and

* Correspondence to: Weigang Road 1, Nanjing 210095, China.

E-mail address: gaoyanzheng@njau.edu.cn (Y. Gao).

¹ ORCID No.: 0000-0002-3814-3555

sustainable treatment solutions to eliminate biotoxins from the environment, i.e. to develop a broad-spectrum degradation system that can degrade a variety of biotoxins.

Advanced oxidation processes (AOPs) based on $\text{SO}_4^{\bullet-}$ have been considered potentially environmentally friendly technologies in water treatment. Compared with traditional $\cdot\text{OH}$ -based AOPs, $\text{SO}_4^{\bullet-}$ exhibit a longer half-life (30–40 μs for $\text{SO}_4^{\bullet-}$, 20 ns for $\cdot\text{OH}$ [15]), which prolongs the continuous contact of $\text{SO}_4^{\bullet-}$ with pollutants and improves degradation efficiency. And $\text{SO}_4^{\bullet-}$ has higher redox potential (2.5–3.1 V) than $\cdot\text{OH}$ (1.8–2.7 V) for contaminants degradation [15]. $\text{SO}_4^{\bullet-}$ can also react 10^3 – 10^5 times faster than conventional oxidants (e.g., H_2O_2 , $\text{Na}_2\text{CO}_3 \cdot 1.5 \text{H}_2\text{O}_2$) and is also more selective for electron-rich pollutants [16]. Persulfate (PS) and peroxymonosulfate (PMS) are commonly used as model superoxides for $\text{SO}_4^{\bullet-}$ production, but PS is more widely used in practical applications than PMS, because PS have higher redox capability ($E^0(\text{S}_2\text{O}_8^{2-}/\text{SO}_4^{\bullet-}) = 1.96 \text{ V}$ [17]), higher $\text{SO}_4^{\bullet-}$ yield and stronger reactivity; And more importantly, commercially available powder products make persulfate inexpensive and easy to store and transport [18]. Therefore, the use of AOPs for broad-spectrum degradation of biotoxins may be a promising green technology with a high treatment efficiency. In AOPs, PS/PMS must be activated to produce reactive oxygen species (ROS), several solid catalysts have been discovered in recent years, for example, Yang et al. activated PMS by MnOx phases and crystals to remove phenolic pollutants [19]; Yao et al. prepared $\text{FeS}_2/\text{C}/\text{PVDF}$ to activate PMS for organics removal [20]. But achieving efficient, stable, and broad-spectrum removal of contaminants by AOPs remains challenging because (i) selective surface active components are lacking to establish strong connections to accelerate interfacial charge transfer; (ii) Due to immature preparation conditions, resulting in the destruction of conjugated systems, the electron shuttle efficiency is low; (iii) The design and regulation of the nanostructure of the heterogeneous catalyst reaction site are not perfect [21]. Therefore, a novel material must be developed as a next generation catalyst to advance the removal of a variety of toxic organics in wastewater treatment.

Layered materials have a good development prospect in water and wastewater treatment. For example, Pelalak et al. summarized the applications of layered double hydroxides (LDHs) material in Fenton-based oxidation processes. Based on the advantages of high surface area, unique exchangeability of intercalated anions, porosity and stable layered structure of catalyst materials, it can be used in Fenton/Fenton-like process to remove phenolic compounds, dyes and others [22]. MXenes are a class of two-dimensional (2D) layered inorganic compounds, such as metal carbides, nitrides, and carbonitrides, it is obtained by selective etching of the intermediate atomic layer of the precursor MAX phase in HF, where M is an early transition metal element (e.g., Ti, V, Nb), A is the third or fourth major group element, X is a C or N element [23]. The structural formula of MXenes is $\text{M}_{n+1}\text{X}_n\text{T}_x$, where T_x is a surface functional group [24]. The layered surface structure, hydrophilic surface, structural flexibility and surface tunable chemistry of MXene make it promising for environmental applications. The application progress of MXene in photocatalysis and $\text{SO}_4^{\bullet-}$ -AOPs was also reviewed by Eghbali et al. [25]. The catalytic degradation performance of MXene (e.g., $\text{Ti}_3\text{C}_2\text{T}_x$, Nb_2CT_x , V_2C)-based catalysts can be improved by inducing binary/multicomponent heterojunctions, metal/nonmetal doping and defect/vacancy engineering, therefore, besides the transition metal electron transfer, MXene-based catalysts may also participate in the degradation of organic pollutants through a combination of different mechanisms [25]. The Ti_3C_2 MXene prepared from Ti_3AlC_2 is a typical graphene-like structural material doped with Ti in MXenes, showing both metallic and nonmetallic properties [23]. Also, there are many hydrophilic functional groups in Ti_3C_2 MXene (e.g., $-\text{O}$, $-\text{OH}$, $-\text{F}$), which can facilitate semiconductor contact. In addition, Ti_3C_2 MXene can lead to a higher redox capacity compared to other carbon materials due to exposed Ti sites and it has been shown to be excellent cocatalyst [26–29], such as Wang et al. reported that $\text{CuS}/\text{Ti}_3\text{C}_2$ MXene nanosheet activates PS for Orange II removal under visible light [30].

Multi-metallic catalysts such as semiconductor spinel ferrite MFe_2O_4 ($\text{M} = \text{Co}$, Cu , Ni , Zn , etc. [31]) has also received widespread attention, for instance, Yu et al. activated PS by $\text{MoS}_2\text{-ZnFe}_2\text{O}_4$ to degrade tetracycline efficiently [32]; the $\text{ZnS-ZnFe}_2\text{O}_4/\text{PS}$ system was fabricated to degrade rhodamine B with a degradation percentage of 97.67% in 90 min [33]. The CoFe_2O_4 are particularly promising for catalysis because of high plasticity and excellent chemical stability. Wu et al. reported that $\text{CoFe}_2\text{O}_{4-x}$ activated PS to degrade bisphenol A with degradation percentages of 26%–98% in 60 min [34]. Moreover, a coupling effect may occur between the two types of metal ions in CoFe_2O_4 , which greatly reduces metal ion leakage [35]. Although CoFe_2O_4 and MXene show certain advantages, but CoFe_2O_4 nanoparticles are prone to aggregation during the preparation process due to its strong magnetism and intermolecular interaction, which greatly reduces its reactive specific surface area [36,37]. For MXenes, (i) there are exposed metal atoms on the surface of MXenes, which are easy oxidized resulting to its structure destroyed; (ii) their mechanical strength is insufficient; (iii) their solubility in non-polar or weakly polar polymers remains challenging [38].

In this regard, the construction of active metals as macro-catalysts on a 2D scale substrate seems to be a sensible solution to overcome the engineering bottleneck mentioned above. CoFe_2O_4 was grown on Ti_3C_2 MXene surface to form a novel nanoparticle/2D nanocomposite material. Multi-metallic $\text{CoFe}_2\text{O}_4/\text{Ti}_3\text{C}_2$ MXene heterojunctions can exploit the superior properties of MXene materials as well as the enhancement effect of metals of CoFe_2O_4 to activate PS. The Ti_3C_2 MXene structure contains more metal active sites by loading CoFe_2O_4 and the surface of $\text{CoFe}_2\text{O}_4/\text{Ti}_3\text{C}_2$ MXene contains hydrophilic functional groups, which can facilitate the diffusion of catalyst in the aqueous matrix, increasing the available reaction sites and the mass transfer of model contaminants [39]. Ti_3C_2 MXene have a layered surface that overcomes their low catalytic efficiency caused by the easy aggregation of CoFe_2O_4 . Although MXene doping technology has been reported for membrane technology and photocatalysis, Ti_3C_2 MXene as a spinel ferrite MFe_2O_4 -doped catalyst carrier for broad-spectrum removal of biotoxins has not been investigated.

Advanced heterogeneous catalysts are necessary to improve PS/PMS activation and the broad-spectrum degradation of a variety of biotoxins. In this study, the CoFe_2O_4 nanoparticles growing on Ti_3C_2 MXene surface to fabricate a multidimensional heterojunction catalyst by hydrothermal method. The results present that the catalytic activity of $\text{CoFe}_2\text{O}_4/\text{Ti}_3\text{C}_2$ MXene for PS is higher than that of CoFe_2O_4 and Ti_3C_2 MXene catalysts. The strong reducing ability of Ti in Ti_3C_2 MXene improves the cycling of $\text{Co(III)}/\text{Co(II)}$ and $\text{Fe(III)}/\text{Fe(II)}$, accelerates the electron transfer process, so lead in promoting the activation of PS and the generation of ROS. Importantly, the $\text{CoFe}_2\text{O}_4/\text{Ti}_3\text{C}_2$ MXene/PS system has a broad-spectrum removal efficiency for a variety of mycotoxins and plants biotoxins, and those biotoxins can be almost completely degraded within 1 h. Finally, the mechanism of electron transfer between $\text{CoFe}_2\text{O}_4/\text{Ti}_3\text{C}_2$ MXene and PS and biotoxins degradation was revealed by combining experiments with quantum chemical calculations. This study provides a new strategy for broad-spectrum removal of a variety of biotoxins by using the growth of ferrites on the surface of MXene to generate free radicals, and sheds new light on the development of biotoxins efficient treatment systems.

2. Experimental section

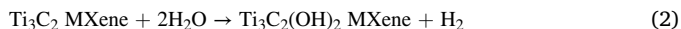
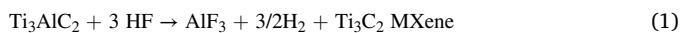
2.1. Materials

The chemicals and reagents used in this study were shown in [Supplementary Material \(SM\)](#).

2.2. Preparation of Ti_3C_2 MXene

The preparation process of Ti_3C_2 MXene and $\text{CoFe}_2\text{O}_4/\text{Ti}_3\text{C}_2$ MXene is shown in [Fig. S1](#). Ti_3C_2 MXene material was prepared by etching

Ti₃AlC₂ MAX with hydrofluoric acid (HF) ($\geq 40\%$). Typically, 1 g Ti₃AlC₂ was added to 20 mL HF in small amounts several times and stirred continuously for 72 h at 25°C. The HF was removed by centrifugation at 3500 rpm, and the precipitates were washed with deionized water until a pH of 6–7 was maintained. The final products were freeze-dried for 24 h. The reaction mechanism follows Eqs. (1) and (2) [40].



2.3. Preparation of multi-metallic catalyst CoFe₂O₄@Ti₃C₂ MXene

CoFe₂O₄@Ti₃C₂ MXene was prepared by first dissolving 0.2481 g Co(NO₃)₂·6 H₂O and 0.4740 g FeSO₄·7 H₂O in 50 mL ethylene glycol. The pH was adjusted to 11 with NaOH. Ti₃C₂ MXene was added and the solution was stirred for 1 h. The mixture was transferred to a hydrothermal reactor at 180°C for 12 h. The solid material after the reaction was washed several times with deionized water and freeze-dried for later use. This dose of raw material can prepare CoFe₂O₄@Ti₃C₂ MXene with a mass:mass ratio of 1:5. By proportionally adjusting the doses of Co(NO₃)₂·6 H₂O, FeSO₄·7 H₂O and Ti₃C₂ MXene, and other conditions remain unchanged, other mass:mass ratios (2:1, 1:1, 1:3, 1:8) of CoFe₂O₄@Ti₃C₂ MXene can be prepared.

2.4. Catalytic performance evaluation

Catalytic oxidation experiments were conducted to identify the catalytic ability and stability of CoFe₂O₄@Ti₃C₂ MXene and the broad-spectrum removal efficiency of CoFe₂O₄@Ti₃C₂ MXene-based system for a variety of biotoxins. The reaction was performed in a 10 mL glass vial with 1 mg L⁻¹ biotoxin solution, which was prepared and initiated by adding 5 mg CoFe₂O₄@Ti₃C₂ MXene and 0.25 mL of 0.04 mol L⁻¹ PS. The reaction solution was oscillated at 200 rpm and 25°C. Aliquots of 0.5 mL were extracted at regular intervals and added 0.5 mL methanol to quench the experiment. The filtration was performed by a 0.22 μm organic phase filter and determined by high-performance liquid chromatography (HPLC, Agilent 1200, USA) analysis. The HPLC conditions are shown in Table S1. All experimental data were collected in triplicate and statistically analyzed using SPSSAU at a 95% confidence level.

2.5. Analytical methods

The detailed methods for characterizing the catalyst and the analytical methods for Brunauer-Emmett-Teller (BET) surface area, vibration sample magnetometer (VSM), total organic carbon (TOC), ion leaching, cyclic voltammetry (CV), electrochemical impedance spectroscopy (EIS), and HPLC—MS are shown in the Supplementary Material (SM). ROS in the CoFe₂O₄@Ti₃C₂ MXene/PS system were trapped using electron paramagnetic resonance (EPR, E500–9.5/12, Bruker, Germany). The ROS capture conditions were C₀ (biotoxin) = 1 mg L⁻¹, C₀ (PS) = 1 mmol L⁻¹, C₀ (CoFe₂O₄@Ti₃C₂ MXene) = 0.5 g L⁻¹, and C₀ (DMPO) = 100 mmol L⁻¹, in which the determination of O₂^{•-} was performed in the DMSO phase.

Apparent kinetics model. The rate equation can be described as Eq. (3) or expressed by logarithms as follows (Eq. (4)):

$$V = (\text{dc}/\text{dt}) = K [\text{Na}_2\text{S}_2\text{O}_8]^a [\text{CoFe}_2\text{O}_4@\text{Ti}_3\text{C}_2 \text{ MXene}]^b \quad (3)$$

$$\lg(\text{dc}/\text{dt}) = \lg K + a \lg [\text{Na}_2\text{S}_2\text{O}_8] + b \lg [\text{CoFe}_2\text{O}_4@\text{Ti}_3\text{C}_2 \text{ MXene}] \quad (4)$$

where K is the total reaction rate constant and a and b are reaction orders. The degradation of biotoxins at different concentrations of Na₂S₂O₈ and fixed doses of CoFe₂O₄@Ti₃C₂ MXene are shown (Fig. S2). The variation in toxin concentration with degradation time was recorded and plotted. The equation was simulated from the curve of

concentration change with time (t : independent variable; c : dependent variable) (Table S2). The derivative of the equation at $t = 0$ is $\lg(\text{dc}/\text{dt})$ at $\lg[\text{CoFe}_2\text{O}_4@\text{Ti}_3\text{C}_2 \text{ MXene}]_0$. Simultaneously, a set of data related to $\lg(\text{dc}/\text{dt})$ versus $\lg[\text{Na}_2\text{S}_2\text{O}_8]_0$ can be obtained. Since the CoFe₂O₄@Ti₃C₂ MXene dose was fixed, $\lg K + b [\text{CoFe}_2\text{O}_4@\text{Ti}_3\text{C}_2 \text{ MXene}]_0$ is a constant. Therefore, $\lg(\text{dc}/\text{dt})$ shows a linear relationship with $\lg[\text{CoFe}_2\text{O}_4@\text{Ti}_3\text{C}_2 \text{ MXene}]_0$. A straight line was obtained by fitting $\lg(\text{dc}/\text{dt})$ to $\lg[\text{CoFe}_2\text{O}_4@\text{Ti}_3\text{C}_2 \text{ MXene}]_0$. The slope is a , and the intercept is $\lg K + b [\text{CoFe}_2\text{O}_4@\text{Ti}_3\text{C}_2 \text{ MXene}]_0$. Similarly, the data of b and $\lg K + a \lg[\text{Na}_2\text{S}_2\text{O}_8]_0$ were obtained. In the case of OTA degradation, the calculation is shown in SM.

The adsorption calculation was performed using all spin-polarized density functional theory (DFT) calculations, in which the Vienna Ab Initio Package (VASP) [41,42] and the Perdew-Burke-Ernzerhof (PBE) [43] formulation within the generalized gradient approximation (GGA) were applied. The specific calculation procedure is shown in the SM. ChemOffice 19.0 was used to draw the biotoxin structures, and optimization by Gaussian 09 W with ωB97XD/6–31 G based on ωB97XD/6–311 G** employed DFT, and simultaneously add SMD solvation model. The optimized frontier molecular orbitals, the highest occupied molecular orbitals (HOMO) and the lowest unoccupied molecular orbitals (LUMO), and the condensed Fukui function were calculated with Multiwfn 3.8 for calculation and are displayed in VMD 1.9.4 [44].

3. Results

3.1. Characterization of the CoFe₂O₄@Ti₃C₂ MXene

SEM show that the precursor, Ti₃AlC₂ MAX, is massive with no obvious stratification in Fig. 1A. SEM and TEM show that Ti₃C₂ MXene prepared according to the method shown in Fig. S1 exhibits a 2D layered structure after etching (Fig. 1A; Fig. S3A). In the TEM lattice fringes of Ti₃C₂ MXene, one crystal plane has a d -value of 1.07 nm, which corresponds to the (002) plane of its MXene phase, and a d -value of 0.27 nm is the (110) plane of XRD analysis (Fig. 1B; Fig. S3B). The CoFe₂O₄ shows a granular structure with a particle diameter of 4.87 nm, and the d -value of 0.26 nm corresponds to the (311) plane of XRD pattern of CoFe₂O₄ (Fig. 1A; Fig. S3B). CoFe₂O₄ adheres to the surface of Ti₃C₂ MXene after the hydrothermal reaction (Fig. 1A). The Ti₃C₂ MXene layered surface is relatively smooth and flat according to TEM images. The loaded CoFe₂O₄ particles on the CoFe₂O₄@Ti₃C₂ MXene surface can be clearly seen, and the crystal plane of CoFe₂O₄ on CoFe₂O₄@Ti₃C₂ MXene has a d -value of 0.29 nm, which corresponds to the (220) plane (Fig. 1B). The corresponding SEM element maps show that the elements of C, Ti, O, Co and Fe were distributed evenly in CoFe₂O₄@Ti₃C₂ MXene (Fig. 1A; Fig. S3C). The selected area electron diffraction (SAED) analysis of the test sample shown in Fig. S3B, the CoFe₂O₄ and CoFe₂O₄@Ti₃C₂ MXene catalysts have polycrystalline properties and exhibit Debye-Scherrer ring patterns, which confirm the structural data of the nanocrystal samples. This result reveals the tight coupling between CoFe₂O₄ and layered Ti₃C₂ MXene, ensuring that the CoFe₂O₄@Ti₃C₂ MXene nanocomposite material was successfully constructed by the hydrothermal synthesis method. XRD detected the crystal characteristics of Ti₃C₂ MXene and its components and the original Ti₃AlC₂. After HF treatment, the diffraction peaks at 38.88° ascribed to (104) dropped sharply, indicating that the Al element was removed. The peaks at 9.04°, 18.46°, 27.78°, 35.16°, 41.76° and 60.68° ascribed to (002), (004), (006), (202), (105) and (110), respectively, are characteristic of Ti₃C₂ MXene [27,45]. The diffraction peaks at 30.00°, 35.38°, 43.16°, 57.14° and 62.78°, corresponding to the (220), (311), (400) (511) and (440) diffraction planes, respectively, are indicative of the CoFe₂O₄ spectrum [46]. After combining CoFe₂O₄ and Ti₃C₂ MXene, the characteristic absorption band attributable to Ti₃C₂ MXene was observed in CoFe₂O₄@Ti₃C₂ MXene (1:5 mass:mass ratio). However, the diffraction peak attributed to CoFe₂O₄ in the nanocomposite is not obvious because of its relatively

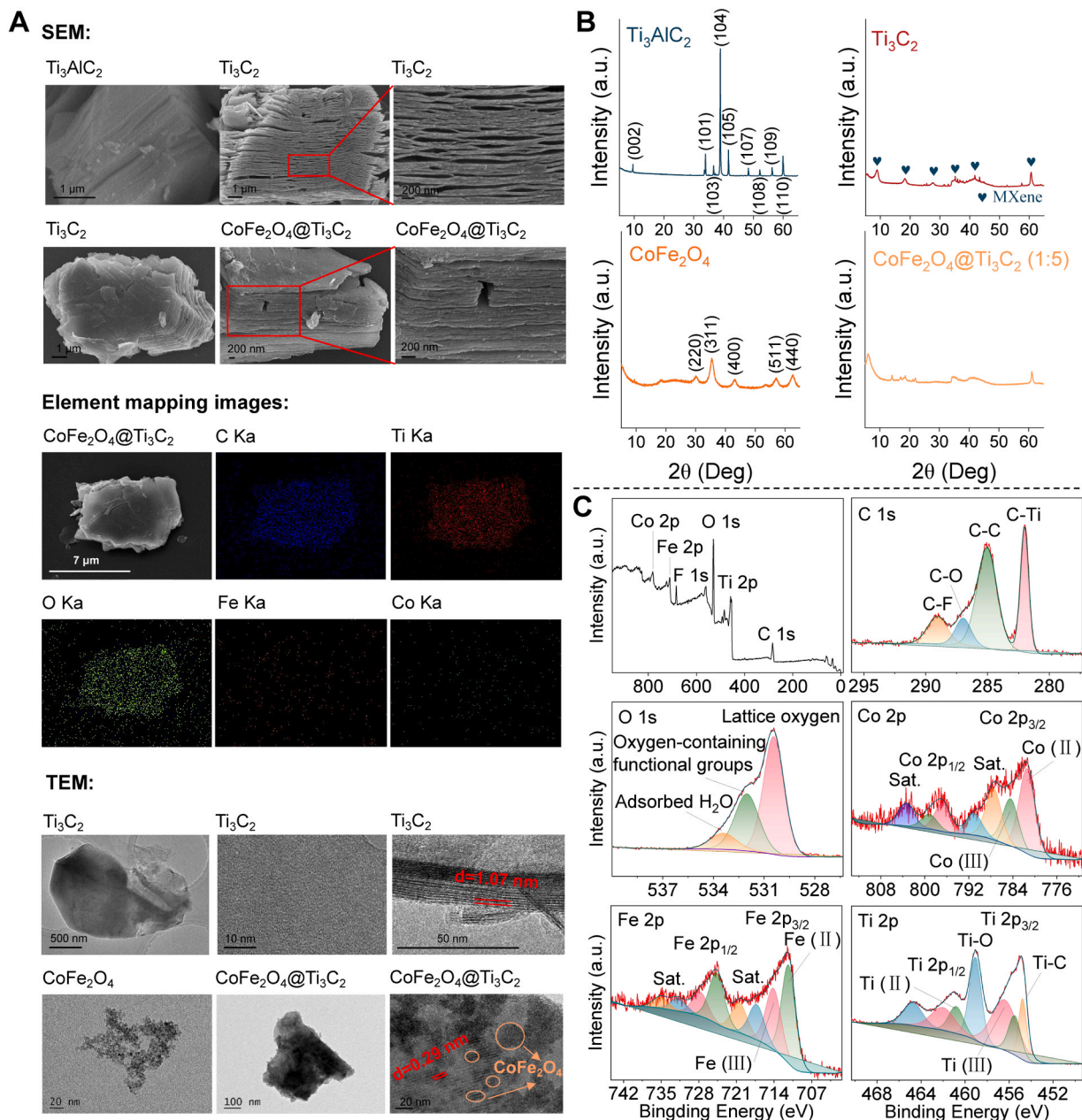


Fig. 1. Characterization of catalyst $\text{CoFe}_2\text{O}_4@\text{Ti}_3\text{C}_2$ MXene. A) SEM images of Ti_3AlC_2 MAX, Ti_3C_2 MXene, and $\text{CoFe}_2\text{O}_4@\text{Ti}_3\text{C}_2$ MXene; Element mapping images of overlay, C, Ti, O, Fe and Co for $\text{CoFe}_2\text{O}_4@\text{Ti}_3\text{C}_2$ MXene; TEM images of Ti_3C_2 MXene, CoFe_2O_4 and $\text{CoFe}_2\text{O}_4@\text{Ti}_3\text{C}_2$ MXene (1:5); B) XRD patterns of Ti_3AlC_2 , Ti_3C_2 MXene, CoFe_2O_4 and $\text{CoFe}_2\text{O}_4@\text{Ti}_3\text{C}_2$ MXene (1:5); C) XPS spectra of fresh $\text{CoFe}_2\text{O}_4@\text{Ti}_3\text{C}_2$ MXene: survey spectra, C 1s spectra, O 1s spectra, Co 2p spectra, Fe 2p spectra and Ti 2p spectra.

low content. In Fig. S4A, the high loading ratio of $\text{CoFe}_2\text{O}_4@\text{Ti}_3\text{C}_2$ MXene (1:1, 2:1 mass:mass ratio) clearly shows the characteristic absorption band of CoFe_2O_4 . In the FT-IR spectrum (Fig. S4B), the peaks at 1640 and 3434 cm^{-1} are related to the stretching and deformation vibrations of the surface hydroxyl group. The VSM curve (Fig. S5A-C) revealed that Ti_3C_2 MXene is extremely weak magnetic, with a magnetic saturation of 0.013 emu g^{-1} . CoFe_2O_4 is strongly ferromagnetic with a magnetic saturation of about 58.24 emu g^{-1} . Whereas $\text{CoFe}_2\text{O}_4@\text{Ti}_3\text{C}_2$ MXene is weakly ferromagnetic with a magnetic saturation of about 0.33 emu g^{-1} , although this value is considered low, it is reasonable because $\text{CoFe}_2\text{O}_4@\text{Ti}_3\text{C}_2$ MXene has a mass:mass ratio of 1:5. The BET measurement results (Fig. S5D-F) indicate that CoFe_2O_4 has a large BET surface area of 215.12 $\text{m}^2 \text{g}^{-1}$, but CoFe_2O_4 has strong ferromagnetism, so it is very easy to agglomerate and has a disadvantage in many chemical reactions. The BET surface area of $\text{CoFe}_2\text{O}_4@\text{Ti}_3\text{C}_2$ MXene (1:5

mass:mass ratio) is greatly increased to 17.24 $\text{m}^2 \text{g}^{-1}$ compared to Ti_3C_2 MXene (8.52 $\text{m}^2 \text{g}^{-1}$). The increased surface area may provide sufficient active sites for PS activation. In addition, the point of zero charge (pHpzc) for $\text{CoFe}_2\text{O}_4@\text{Ti}_3\text{C}_2$ MXene was 4.08 (Fig. S6). This indicates that $\text{CoFe}_2\text{O}_4@\text{Ti}_3\text{C}_2$ MXene may be affected by the initial pH value of the solution, and at initial solution pH values lower than 4.08, more positive charges on its surface may be enriched, which favors reaction with $\text{S}_2\text{O}_8^{2-}$.

The composition and morphology of surface elements for fresh $\text{CoFe}_2\text{O}_4@\text{Ti}_3\text{C}_2$ MXene were analyzed by XPS (Fig. 1C). Co, Fe, F, O, Ti and C coexist in $\text{CoFe}_2\text{O}_4@\text{Ti}_3\text{C}_2$ MXene, and the relative content is listed in Table S3. Additionally, the binding energies of important peaks for each element are listed in Table S4 for C and O, Table S5 for Co, Table S6 for Fe, and Table S7 for Ti. The binding energies of 282.00, 285.02, 286.95 and 289.04 eV in the C1s spectrum correspond to C-Ti,

C-C, C-O and C-F, respectively [27]. The element O was found in three peaks (530.42, 531.99 and 533.40 eV), which are related to lattice oxygen, oxygen-containing functional groups and adsorbed H₂O [47]. The Co 2p and Fe 2p XPS spectra include Co 2p_{3/2} and Co 2p_{1/2}, Fe 2p_{3/2} and Fe 2p_{1/2}, respectively, as well as satellite peaks. The peaks of Co(II) species are at 781.35 eV and 796.71 eV, while the peaks of Co(III) species are at 784.34 eV and 799.15 eV. The Fe 2p_{3/2} peak positions of Fe(II) and Fe(III) are located at 711.24 eV and 714.03 eV, respectively, and the corresponding Fe 2p_{1/2} peak positions appear at 724.61 eV and 727.73 eV. Ti 2p can be divided into seven peaks at 454.73, 455.45, 456.37, 459.03, 460.78, 461.98 and 464.72 eV, which are Ti-C, Ti(II) 2p_{3/2}, Ti(III) 2p_{3/2}, Ti-O 2p_{3/2}, Ti(II) 2p_{1/2}, Ti(III) 2p_{1/2} and Ti-O 2p_{1/2}, respectively.

3.2. Performance of CoFe₂O₄@Ti₃C₂ MXene in PS activation for biotoxin broad-spectrum degradation

The catalytic activity of CoFe₂O₄@Ti₃C₂ MXene in PS activation was evaluated based on the degradation of OTA, OTB, OTC, AFB₁, AFB₂, AFG₁, AFG₂, AFM₁, AFM₂, GT, DON, BEAU, POD and XAT. As shown in Fig. 2A, the residual content of biotoxin was detected by HPLC, as shown in Table S1, and the CoFe₂O₄@Ti₃C₂ MXene/PS system was very efficient in degrading biotoxins. All biotoxins except OTB and POD were completely degraded within 50 min, and the OTB and POD degradation percentages were 93.34% and 88.15%, respectively. The apparent rate constant, *K*, for the degradation of OTB and POD was calculated as 0.55 and 0.02, respectively (Eqs. (5) and (6)). Among them, AFG₁ and AFG₂ were removed within 5 min, and the *K* for AFG₁ and AFG₂ were 2.01 and 1.20, respectively (Eqs. (7) and (8)). The apparent reaction rate

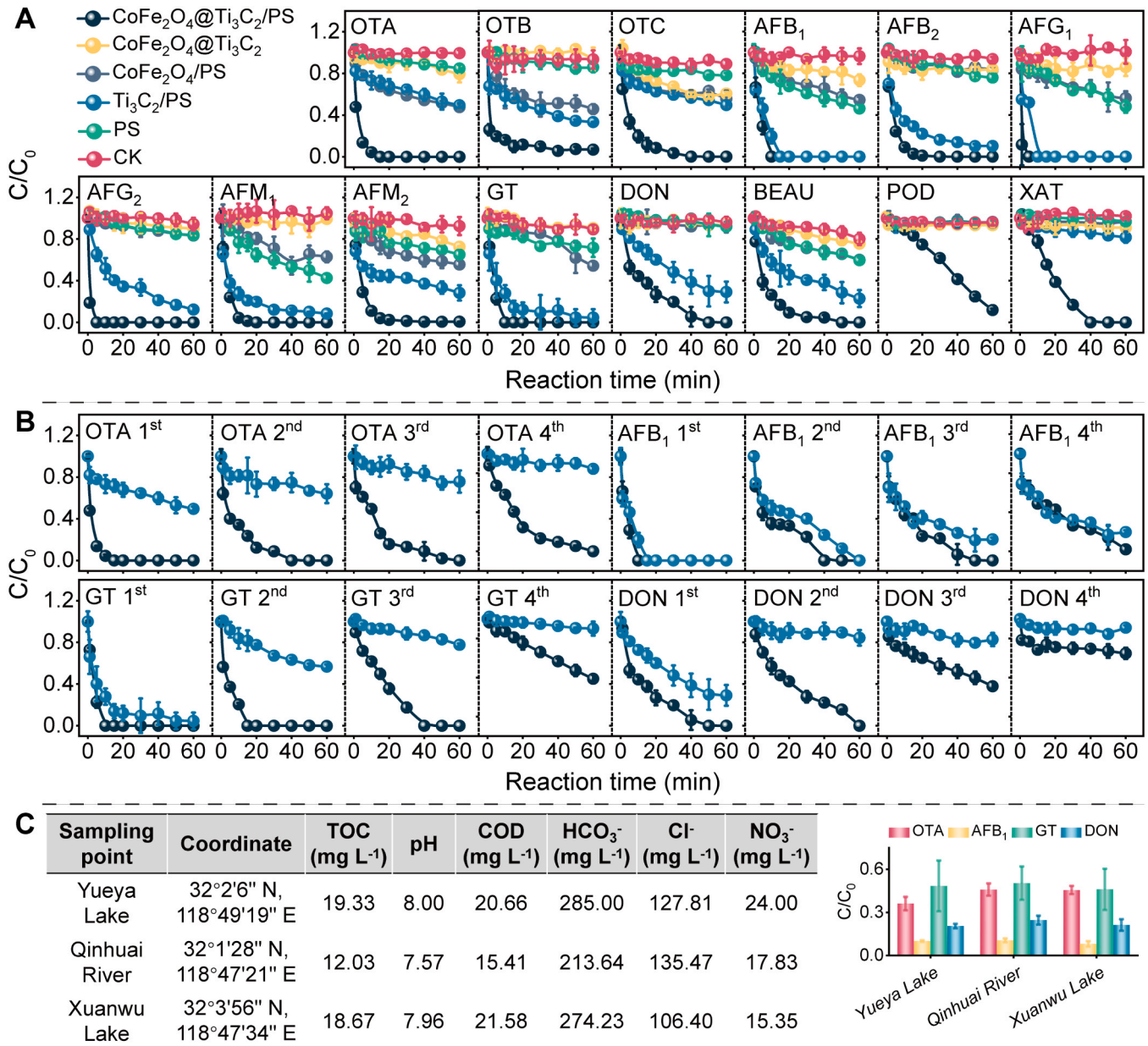


Fig. 2. The degradation of biotoxins. A) The degradation of biotoxins in CoFe₂O₄@Ti₃C₂ MXene/PS system. CK indicates the control treatment without PS and CoFe₂O₄@Ti₃C₂ MXene. B) OTA, AFB₁, GT and DON degradation in four consecutive cycles by CoFe₂O₄@Ti₃C₂ MXene/PS oxidation system. C) Sampling location and physicochemical characteristics for natural water bodies of Yueya lake, Qinhuai river and Xuanwu lake, and the removal of OTA, AFB₁, GT and DON in the natural water environment. Conditions: C₀ (biotoxin) = 1 mg L⁻¹, C₀ (PS) = 1 mmol L⁻¹, C₀ (catalyst) = 0.5 g L⁻¹, initial pH unadjusted, 25°C.

equations of other biotoxins are shown in Table 1.

$$V = dc/dt = 0.55[\text{Na}_2\text{S}_2\text{O}_8]^{1.1899} [\text{CoFe}_2\text{O}_4@\text{Ti}_3\text{C}_2 \text{ MXene}]^{1.3534} \quad (5)$$

$$V = dc/dt = 0.02[\text{Na}_2\text{S}_2\text{O}_8]^{0.8683} [\text{CoFe}_2\text{O}_4@\text{Ti}_3\text{C}_2 \text{ MXene}]^{0.9224} \quad (6)$$

$$V = dc/dt = 2.01[\text{Na}_2\text{S}_2\text{O}_8]^{0.7376} [\text{CoFe}_2\text{O}_4@\text{Ti}_3\text{C}_2 \text{ MXene}]^{1.0455} \quad (7)$$

$$V = dc/dt = 1.20[\text{Na}_2\text{S}_2\text{O}_8]^{1.0139} [\text{CoFe}_2\text{O}_4@\text{Ti}_3\text{C}_2 \text{ MXene}]^{0.5848} \quad (8)$$

$\text{CoFe}_2\text{O}_4@\text{Ti}_3\text{C}_2$ MXene exerts different adsorption effects on biotoxins. The adsorption capacity for OTA, OTB, OTC, AFB₁, AFB₂, AFG₁, AFG₂, AFM₁, AFM₂, GT, DON, BEAU, POD and XAT were 20.57%, 6.58%, 39.53%, 26.63%, 16.12%, 14.02%, 10.09%, 0.75%, 27.42%, 24.50%, 9.60%, 6.14%, 6.68% and 9.09%, respectively. Interestingly, the control group containing Ti_3C_2 MXene/PS also exhibited biotoxin degradation. With the exception of POD and XAT, the degradation percentage was above 50%. $\text{CoFe}_2\text{O}_4/\text{PS}$ resulted in removal percentages above 40% for OTA, OTB, OTC, AFB₁, AFG₁, AFM₂, GT and BEAU. Other details about the control groups are provided in SM.

The molecular frontier orbital of each biotoxin, which were calculated based on DFT, are shown in Fig. 3A. The order of the highest occupied molecular orbital (HOMO) energies is $\text{DON} < \text{OTB} < \text{OTC} < \text{OTA} < \text{BEAU} < \text{AFM}_1 < \text{AFM}_2 < \text{AFG}_1 < \text{AFG}_2 < \text{AFB}_1 < \text{AFB}_2 < \text{GT} < \text{XAT} < \text{POD}$, and the order of the lowest unoccupied molecular orbital (LUMO) energies is $\text{AFM}_1 < \text{AFG}_1 < \text{AFG}_2 < \text{AFM}_2 < \text{AFB}_1 < \text{AFB}_2 < \text{OTA} < \text{OTC} < \text{DON} < \text{XAT} < \text{OTB} < \text{GT} < \text{BEAU} < \text{POD}$. The HOMO-LUMO gaps of OTA, OTB, OTC, AFB₁, AFB₂, AFG₁, AFG₂, AFM₁, AFM₂, GT, DON, BEAU, POD and XAT were 4.5782, 4.7702, 4.5828, 3.9668, 3.9863, 3.8781, 3.9003, 4.1087, 4.0678, 4.3514, 4.8272, 5.7549, 5.3214 and 3.9910 eV, respectively. Pearson correlation analysis was conducted between the K values of biotoxins degradation in the $\text{CoFe}_2\text{O}_4@\text{Ti}_3\text{C}_2$ MXene/PS system and the HOMO-LUMO gap of biotoxins, and the results showed a significant negative correlation ($p < 0.05$), with a correlation coefficient of 0.634 (Fig. 3B).

To further explore the reusability of $\text{CoFe}_2\text{O}_4@\text{Ti}_3\text{C}_2$ MXene, four representative biotoxins, namely, OTA, AFB₁, GT, and DON, were selected for degradation experiments (Fig. 2B). The treatment details of

Table 1

The apparent kinetics equation for the degradation of fourteen biotoxins in $\text{CoFe}_2\text{O}_4@\text{Ti}_3\text{C}_2$ MXene/PS system.

Biotoxin	Apparent kinetics equation	K
OTA	$V = dc/dt = 0.45[\text{Na}_2\text{S}_2\text{O}_8]^{0.9300} [\text{CoFe}_2\text{O}_4@\text{Ti}_3\text{C}_2 \text{ MXene}]^{0.8779}$	0.45
OTB	$V = dc/dt = 0.55[\text{Na}_2\text{S}_2\text{O}_8]^{1.1899} [\text{CoFe}_2\text{O}_4@\text{Ti}_3\text{C}_2 \text{ MXene}]^{1.3534}$	0.55
OTC	$V = dc/dt = 0.53[\text{Na}_2\text{S}_2\text{O}_8]^{0.8192} [\text{CoFe}_2\text{O}_4@\text{Ti}_3\text{C}_2 \text{ MXene}]^{1.4571}$	0.53
AFB ₁	$V = dc/dt = 0.96[\text{Na}_2\text{S}_2\text{O}_8]^{2.1699} [\text{CoFe}_2\text{O}_4@\text{Ti}_3\text{C}_2 \text{ MXene}]^{1.0867}$	0.96
AFB ₂	$V = dc/dt = 0.73[\text{Na}_2\text{S}_2\text{O}_8]^{0.9976} [\text{CoFe}_2\text{O}_4@\text{Ti}_3\text{C}_2 \text{ MXene}]^{1.3977}$	0.73
AFG ₁	$V = dc/dt = 2.01[\text{Na}_2\text{S}_2\text{O}_8]^{0.7376} [\text{CoFe}_2\text{O}_4@\text{Ti}_3\text{C}_2 \text{ MXene}]^{1.0455}$	2.01
AFG ₂	$V = dc/dt = 1.20[\text{Na}_2\text{S}_2\text{O}_8]^{1.0139} [\text{CoFe}_2\text{O}_4@\text{Ti}_3\text{C}_2 \text{ MXene}]^{0.5848}$	1.20
AFM ₁	$V = dc/dt = 0.81[\text{Na}_2\text{S}_2\text{O}_8]^{0.8064} [\text{CoFe}_2\text{O}_4@\text{Ti}_3\text{C}_2 \text{ MXene}]^{1.3158}$	0.81
AFM ₂	$V = dc/dt = 0.53[\text{Na}_2\text{S}_2\text{O}_8]^{0.6128} [\text{CoFe}_2\text{O}_4@\text{Ti}_3\text{C}_2 \text{ MXene}]^{1.2476}$	0.53
GT	$V = dc/dt = 0.41[\text{Na}_2\text{S}_2\text{O}_8]^{1.9138} [\text{CoFe}_2\text{O}_4@\text{Ti}_3\text{C}_2 \text{ MXene}]^{1.1783}$	0.41
DON	$V = dc/dt = 0.03[\text{Na}_2\text{S}_2\text{O}_8]^{1.4174} [\text{CoFe}_2\text{O}_4@\text{Ti}_3\text{C}_2 \text{ MXene}]^{0.0738}$	0.03
BEAU	$V = dc/dt = 0.10[\text{Na}_2\text{S}_2\text{O}_8]^{1.0341} [\text{CoFe}_2\text{O}_4@\text{Ti}_3\text{C}_2 \text{ MXene}]^{1.2174}$	0.10
POD	$V = dc/dt = 0.02[\text{Na}_2\text{S}_2\text{O}_8]^{0.8683} [\text{CoFe}_2\text{O}_4@\text{Ti}_3\text{C}_2 \text{ MXene}]^{0.9224}$	0.02
XAT	$V = dc/dt = 0.06[\text{Na}_2\text{S}_2\text{O}_8]^{1.3275} [\text{CoFe}_2\text{O}_4@\text{Ti}_3\text{C}_2 \text{ MXene}]^{1.4415}$	0.06

the $\text{CoFe}_2\text{O}_4@\text{Ti}_3\text{C}_2$ MXene before reuse are shown in SM. The degradation percentages of AFB₁, GT and DON decreased from 100% to 98%, 61% and 35% after $\text{CoFe}_2\text{O}_4@\text{Ti}_3\text{C}_2$ MXene was used for four cycles, while OTA was completely degraded in all four cycles. GT was completely degraded when $\text{CoFe}_2\text{O}_4@\text{Ti}_3\text{C}_2$ MXene was used for three or fewer cycles, and DON could only be completely removed when $\text{CoFe}_2\text{O}_4@\text{Ti}_3\text{C}_2$ MXene was used for two cycles or less.

In addition, three real water samples from Nanjing, China, were collected to determine the effect of $\text{CoFe}_2\text{O}_4@\text{Ti}_3\text{C}_2$ MXene on PS activation for the degradation of OTA, AFB₁, GT and DON under natural water conditions. The water samples were collected from Yueya Lake, the Qinhuai River and Xuanwu Lake, and the sampling coordinates are shown in Fig. 2C. The practical application of AOPs was influenced by physical and chemical properties of water. The physicochemical characteristics of the three water bodies, such as pH value, TOC, COD, HCO_3^- , Cl^- and NO_3^- content, were analyzed, as shown in Fig. 2C. All three kinds of water bodies are alkaline. The TOC content of Yueya Lake, the Qinhuai River and Xuanwu Lake was 19.33, 12.03 and 18.67 mg L⁻¹, respectively. The concentrations of COD, HCO_3^- , Cl^- and NO_3^- were 15.41–21.58, 213.64–285.00, 106.40–135.47 and 15.35–24.00 mg L⁻¹, respectively. The removal efficiency was reduced in all environmental samples. The degradation percentages in the three real water bodies were 63.88%, 54.10%, and 54.42% for OTA; 89.93%, 89.49%, and 91.94% for AFB₁; 51.56%, 49.61%, and 53.91% for GT; and 79.53%, 75.40%, and 78.81% for DON.

The mineralization extent of biotoxins was also analyzed by TOC in optimum conditions (Fig. S7) in SM. Other factors, including $\text{CoFe}_2\text{O}_4@\text{Ti}_3\text{C}_2$ MXene dosage and PS concentration (Fig. S2), initial pH, oxidant type, inorganic anions (Fig. S8), and high contamination concentration of biotoxins (Fig. S9), were explored. The detailed results and discussion are shown in SM.

3.3. Mechanistic study

To investigate the catalytic role of $\text{CoFe}_2\text{O}_4@\text{Ti}_3\text{C}_2$ MXene, the mechanism of the generated ROS in the catalytic process was studied. Some ROS, such as $\text{SO}_4^{\bullet-}$ and $\bullet\text{OH}$, show strong oxidizing ability, and their reaction rates with pollutants have been observed at 10^6 – 10^9 M⁻¹s⁻¹ [15,48]. Four representative biotoxin degradation systems (OTA, AFB₁, GT, and DON) were used to determine the ROS. As shown in Fig. 4A, B and Fig. S10A, EPR was applied to directly measure the ROS in the $\text{CoFe}_2\text{O}_4@\text{Ti}_3\text{C}_2$ MXene/PS system within 0–20 min. Strong DMPO- $\bullet\text{OH}$ (hyperfine coupling constants of $\alpha_N = \alpha_H = 14.8$ G) adduct signal peaks with the intensity ratio of 1:2:2:1, DMPO- $\text{O}_2^{\bullet-}$ ($\alpha_N = 14.0$ G, $\alpha_H = 12.9$ G) adduct signal peaks with the intensity ratio of 1:1:1:1, and TEMP- $\text{O}_2^{\bullet-}$ ($\alpha_N = 16.9$ G) adduct signal peaks with the intensity ratio of 1:1:1 were observed, while DMPO- $\text{SO}_4^{\bullet-}$ ($\alpha_N = 13.2$ G, $\alpha_H = 9.6$ G, $\alpha_H = 1.48$ G, and $\alpha_H = 0.78$ G) signal with the intensity ratio of 1:1:1:1:1:1 was not obvious. In this work, EtOH, TBA, p-BQ and FFA were employed as scavengers for $\text{SO}_4^{\bullet-} + \bullet\text{OH}$, $\bullet\text{OH}$, $\text{O}_2^{\bullet-}$ and O_2 , respectively. As displayed in Fig. S11, the addition of scavengers inhibited the catalytic performance and the degradation rate of each biotoxin was reduced to varying degrees. Except for AFB₁, AFG₁, GT and XAT, the degradation percentage of all biotoxins in the presence of EtOH, TBA and p-BQ dropped below 50%. The degradation percentages of AFB₁ in the EtOH- and TBA-quenched systems were 72.61% and 74.92%, respectively. The percent degradation of AFG₁, GT and XAT in the presence of TBA was 51.40%, 81.84% and 54.75%, respectively. However, FFA has little effect on the degradation of the four biotoxins, and the final degradation rate of biotoxins can still reach 100% (Fig. S10B–E), so O_2 may have no contributions for biotoxins degradation. The apparent rate constant, K , of each biotoxin was correspondingly reduced, as shown in Fig. 4C.

The contribution of each ROS to biotoxin degradation was evaluated by the effect of adding each respective scavenger alone. The specific contribution of each ROS was calculated according to formula (9) [49, 50].

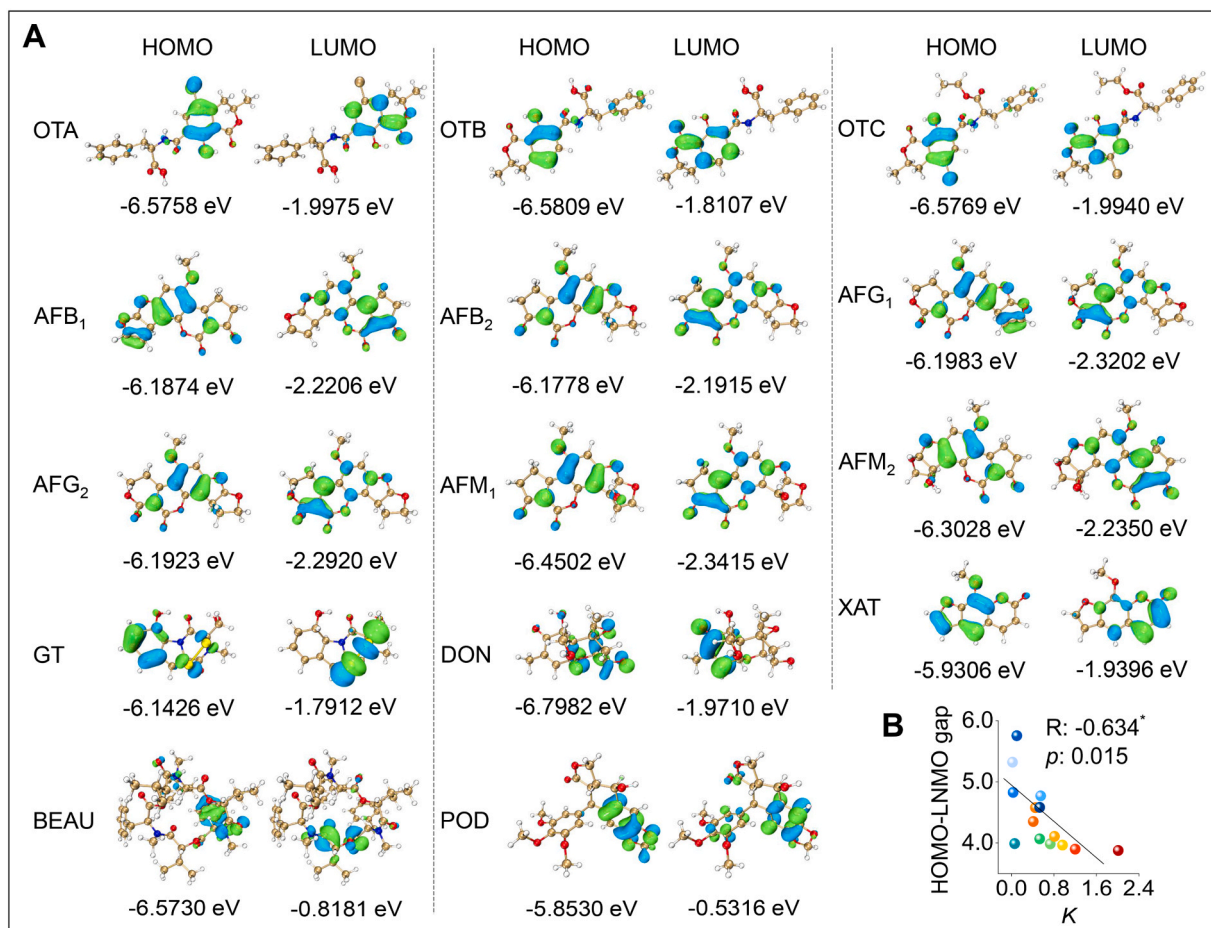


Fig. 3. Molecular frontier orbital and correlation analysis. **A)** The highest occupied molecular orbital (HOMO) and the lowest unoccupied molecular orbital (LUMO) of biotoxins based on density functional theory (DFT). **B)** the linear fit between the biotoxins reaction rate constant K and HOMO-LUMO gap, where R and p are the correlation coefficient and significance level obtained by Pearson correlation analysis, respectively.

$$R = (K_{app} - K_r)/K_{app} \quad (9)$$

where R (%) is the contribution percentage of ROS to biotoxin degradation, K_{app} (min^{-1}) is the apparent rate constant of each biotoxin degradation in the absence of scavenger, and K_r (min^{-1}) is the apparent rate constant of each biotoxin degradation in the presence of scavenger.

The contributions for each ROS in the presence of a scavenger alone were shown in Fig. 4C, when the reactivity of each ROS scavenger on other ROS are not considered, the contributions were $\cdot\text{OH} \approx \text{O}_2^{\cdot-} > \text{SO}_4^{\cdot-}$ for OTA, OTB, OTC, AFB₁, AFB₂, AFG₁, AFG₂, AFM₁, AFM₂ and BEAU; $\text{O}_2^{\cdot-} > \cdot\text{OH} > \text{SO}_4^{\cdot-}$ for GT, POD and XAT; and $\cdot\text{OH} > \text{O}_2^{\cdot-} > \text{SO}_4^{\cdot-}$ for DON. The tendency of decomposition based on the PS concentration was also determined for the four degradation systems shown in Fig. 4D to further demonstrate that the generation of ROS originates from the decomposition of PS. The concentration of PS decreased from 1 mmol L^{-1} to 0.34, 0.28, 0.21 and 0.22 mmol L^{-1} for the OTA, AFB₁, GT and DON degradation systems, respectively.

To study the interaction and potential synergistic effects between the components of $\text{CoFe}_2\text{O}_4/\text{Ti}_3\text{C}_2$ MXene and to analyze the surface chemical state of elements, XPS was performed on the $\text{CoFe}_2\text{O}_4/\text{Ti}_3\text{C}_2$ MXene nanocomposite after one and four cycles of OTA, AFB₁, GT and DON degradation. The elemental composition of $\text{CoFe}_2\text{O}_4/\text{Ti}_3\text{C}_2$ MXene (C, O, Co, Fe, Ti and F) did not change throughout the four cycles (Fig. 5; Fig. S12). The elemental content, the binding energy corresponding to the fitting peak of each element, and the percentage of some elements in different valence states are listed in Tables S3-S7. Compared with fresh $\text{CoFe}_2\text{O}_4/\text{Ti}_3\text{C}_2$ MXene, the contents of Co and Fe were

reduced throughout cycling (Fig. 5; Fig. S12; Table S3, S5-S6). In Fig. 5 and Table S5-S6, the content of Fe(II) was significantly reduced from 41.64% to 31.23%, 34.71%, 36.79% and 39.69%, while Fe(III) was significantly increased from 22.75% to 30.40%, 28.18%, 25.94% and 23.26% in the OTA, AFB₁, GT and DON degradation systems. Interestingly, the Fe(II) content increased from 44.09% to 46.93%, 46.89%, 48.78% and 46.33%, while Fe(III) decreased from 27.23% to 25.81%, 25.23%, 23.84% and 26.37% in the four systems after one cycle. As displayed in Fig. S12 and Table S5-S6, $\text{CoFe}_2\text{O}_4/\text{Ti}_3\text{C}_2$ MXene was also analyzed after four cycles. The content of Fe(II) increased to 33.49%, 41.66%, 42.18% and 32.84%, and Fe(III) decreased to 27.77%, 26.05%, 22.89% and 27.15% in the degradation systems of OTA, AFB₁, GT and DON, respectively. The Fe(II) content continued to increase in the OTA, GT and DON degradation systems (46.95%, 52.91% and 49.86%, respectively) but decreased to 43.41% in the AFB₁ system. The Fe(III) content also continued to decrease to 23.92%, 24.22%, 22.94% and 22.56% for the OTA, AFB₁, GT and DON degradation systems, respectively. It should be pointed out that, the content changes in Fe(II) and Fe(III) were nonlinear with respect to cycle number. As displayed in Fig. 5, Fig. S12 and Table S7, Ti has three valence states: Ti(II) , Ti(III) , Ti(IV) in this MXene, after four cycles, the Ti-O content continued to increase from 30.91% to 35.99%, 31.74%, 40.14% and 35.16% for the OTA, AFB₁, GT and DON degradation systems, while the Ti(II) content continued to decrease in the four systems, which were 24.64%, 25.78%, 22.03% and 23.72%, respectively.

The interaction between $\text{CoFe}_2\text{O}_4/\text{Ti}_3\text{C}_2$ MXene and PS was further explored, and the adsorption of Co, Fe and Ti sites on $\text{CoFe}_2\text{O}_4/\text{Ti}_3\text{C}_2$

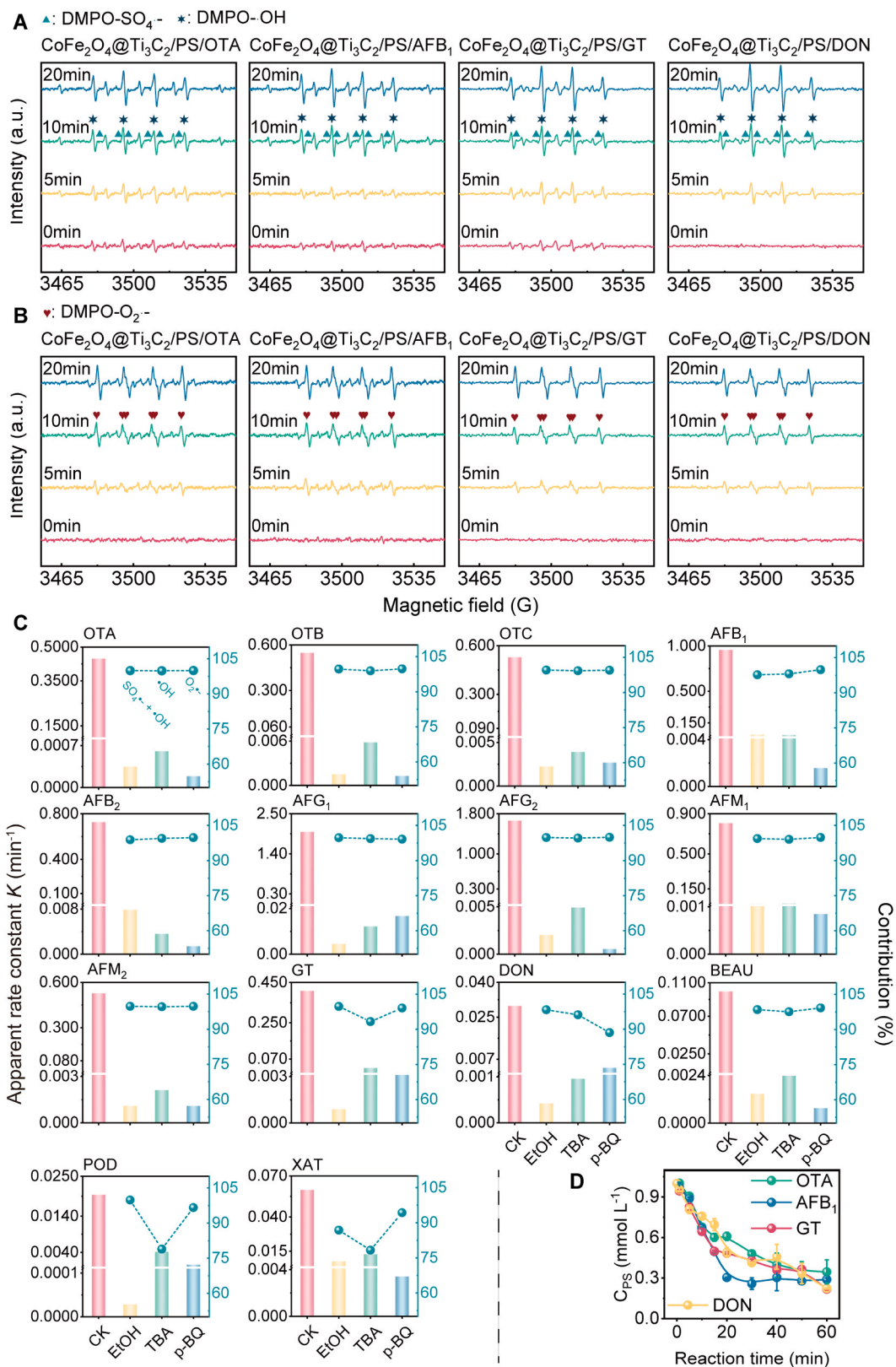


Fig. 4. Determination and contribution of reactive oxygen species (ROS). **A**) Determination of ROS by EPR in the CoFe₂O₄@Ti₃C₂ MXene/PS/(OTA, AFB₁, GT and DON) systems. **B**) The effects of scavengers (TBA, EtOH and p-BQ). **C**) The contribution of reactive species for the degradation of biotoxins in the CoFe₂O₄@Ti₃C₂ MXene/PS system. **D**) The concentration of PS in the CoFe₂O₄@Ti₃C₂ MXene/PS/(OTA, AFB₁, GT and DON) systems. CK indicates the control treatment without scavengers. Conditions: C₀ (biotoxin) = 1 mg L⁻¹, C₀ (PS) = 1 mmol L⁻¹, C₀ (catalyst) = 0.5 g L⁻¹, C₀ (DMPO) = 100 mmol L⁻¹, C₀ (EtOH/TBA) = 500 mmol L⁻¹, C₀ (p-BQ) = 10 mmol L⁻¹, initial pH unadjusted, 25°C.

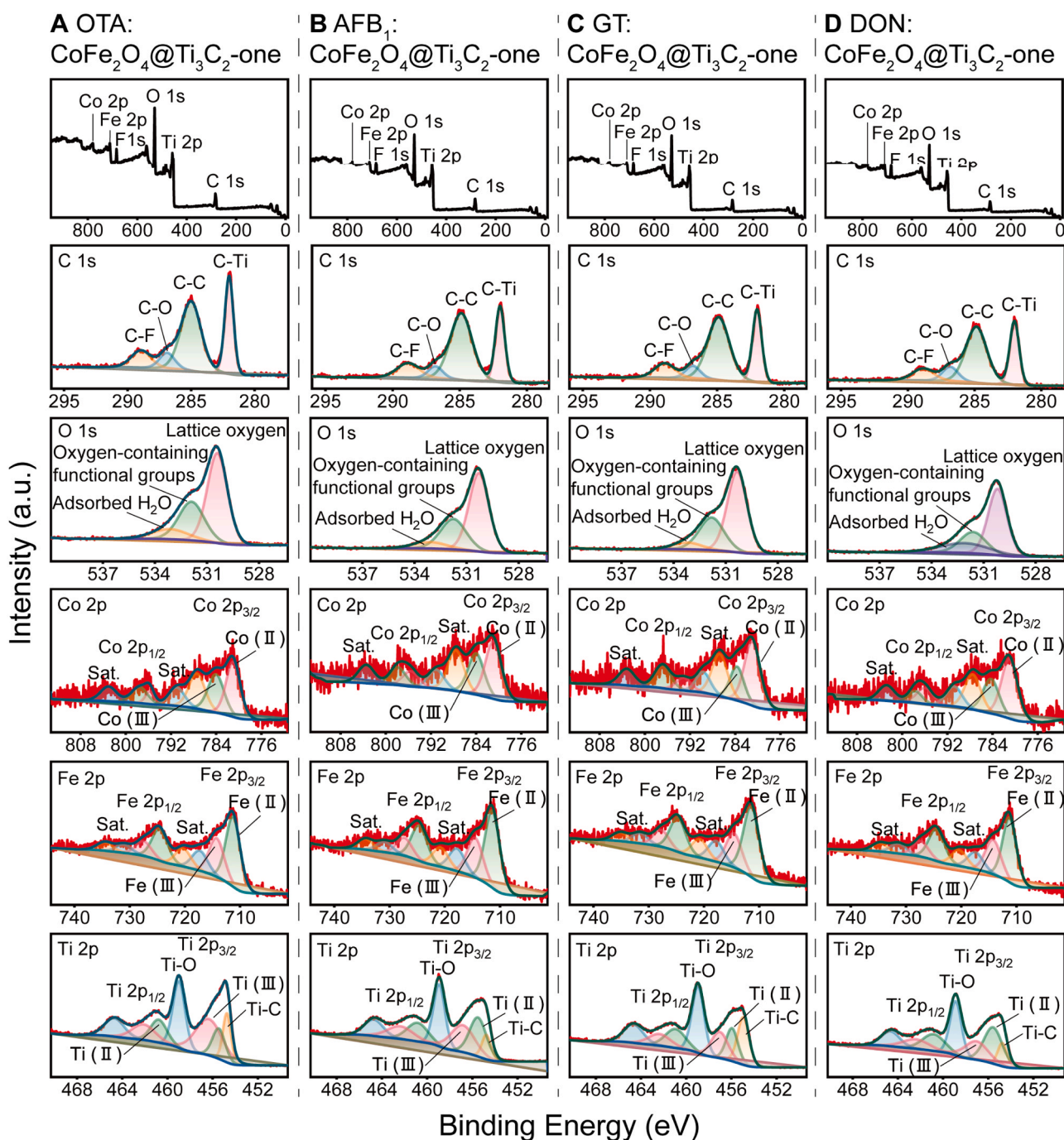


Fig. 5. Element valence analysis. XPS spectra of used $\text{CoFe}_2\text{O}_4/\text{Ti}_3\text{C}_2$ MXene in A) OTA, B) AFB₁, C) GT and D) DON degradation systems, including survey spectra, C 1 s, O 1 s, Co 2p, Fe 2p and Ti 2p.

MXene and $\text{S}_2\text{O}_8^{2-}$ molecules was calculated on the basis of DFT. The Co site (Fig. 6A) exhibited the strongest adsorption capacity for $\text{S}_2\text{O}_8^{2-}$, with an adsorption energy (E_{ad}) of -21.15 eV and an amount of electron transfer (Q) of 1.458 e. This was followed by Fe sites (Fig. 6B) with an E_{ad} of -19.63 eV and a Q of 1.467 e. In addition, the O-O bond lengths increased from the original 1.497 Å to 1.506 Å and 1.501 Å after $\text{S}_2\text{O}_8^{2-}$ was adsorbed on $\text{CoFe}_2\text{O}_4/\text{Ti}_3\text{C}_2$ MXene via Co and Fe sites, which facilitated subsequent O-O bond cleavage. The Ti site (Fig. 6C) on $\text{CoFe}_2\text{O}_4/\text{Ti}_3\text{C}_2$ MXene exhibited a lower E_{ad} for $\text{S}_2\text{O}_8^{2-}$ of -7.55 eV but a higher Q (3.443 e) due to the strong reducing ability of Ti on Ti_3C_2 MXene. $\text{S}_2\text{O}_8^{2-}$ directly decomposed into two SO_4 groups on the surface of $\text{CoFe}_2\text{O}_4/\text{Ti}_3\text{C}_2$ MXene. The SO_4 was bound to the surface through Ti-O covalent bonds, and according to the XPS results, converting SO_4

groups to $\text{SO}_4^{\bullet-}$ may be difficult to perform. The adsorption capacity of Ti_3C_2 MXene (Ti sites) for $\text{S}_2\text{O}_8^{2-}$ was also analyzed (Fig. 6D). Similar to the Ti site of $\text{CoFe}_2\text{O}_4/\text{Ti}_3\text{C}_2$ MXene, $\text{S}_2\text{O}_8^{2-}$ is directly decomposed into SO_4 groups, but the adsorption capacity (E_{ad} : -2.29 eV, Q : 3.386 e) was very low. Therefore, Co and Ti were the main sites for $\text{CoFe}_2\text{O}_4/\text{Ti}_3\text{C}_2$ MXene to trigger PS activation.

CV and EIS were conducted to analyze the ability of the catalyst to transfer electrons. As shown in Fig. 6E, significantly stronger redox peaks were observed in $\text{CoFe}_2\text{O}_4/\text{Ti}_3\text{C}_2$ MXene than in CoFe_2O_4 and Ti_3C_2 MXene. Moreover, the difference in charge potential of $\text{CoFe}_2\text{O}_4/\text{Ti}_3\text{C}_2$ MXene is larger, and the cycle reversibility is better. The large surface area in CV suggested that the surface of $\text{CoFe}_2\text{O}_4/\text{Ti}_3\text{C}_2$ MXene contains numerous active centers. Notably, in

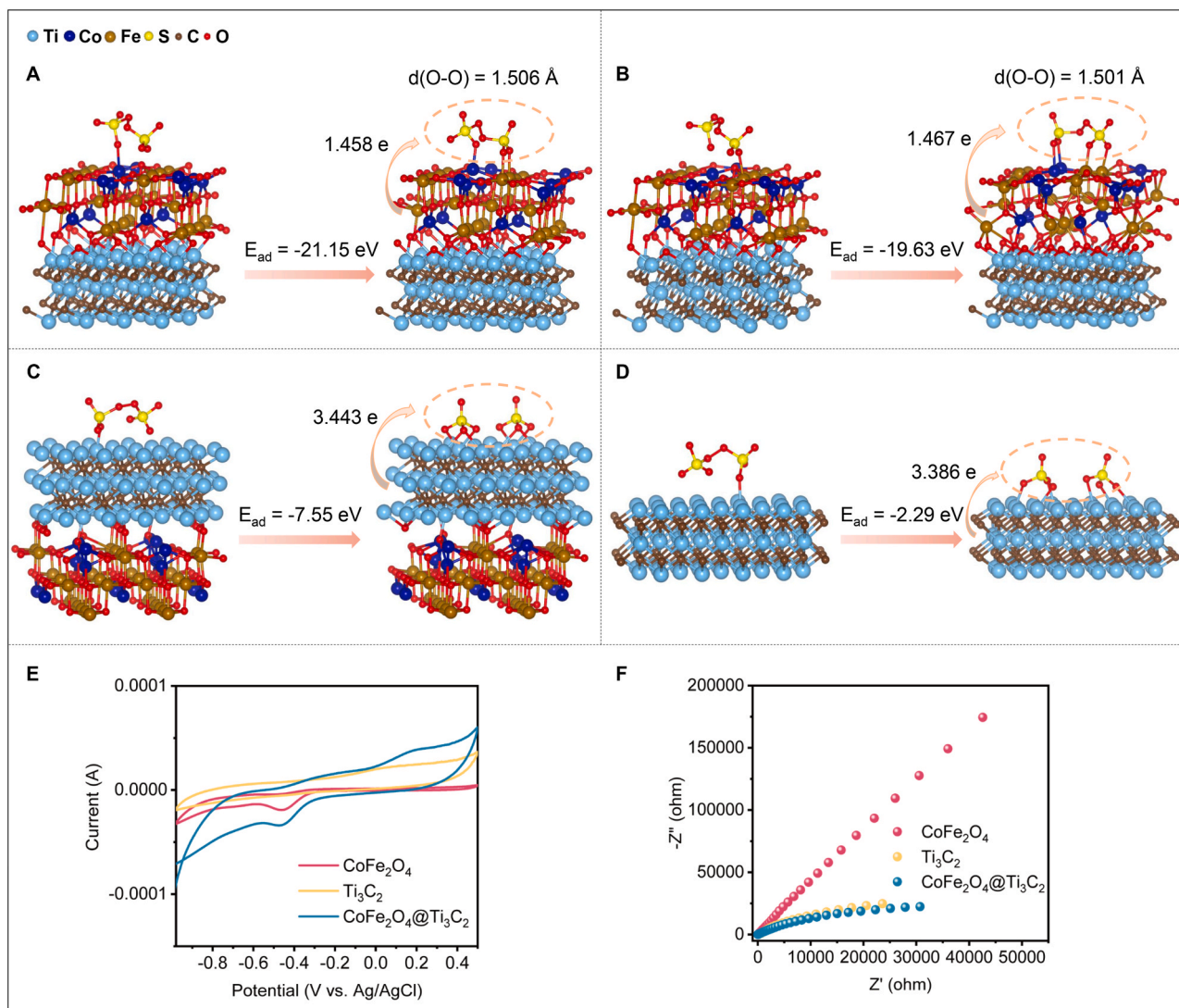


Fig. 6. The adsorption energy calculation and electron transfer capability. **A)** $\text{S}_2\text{O}_8^{2-}$ binding to Co sites on $\text{CoFe}_2\text{O}_4@\text{Ti}_3\text{C}_2$ MXene. **B)** $\text{S}_2\text{O}_8^{2-}$ binding to Fe sites on $\text{CoFe}_2\text{O}_4@\text{Ti}_3\text{C}_2$ MXene. **C)** $\text{S}_2\text{O}_8^{2-}$ binding to Ti sites on $\text{CoFe}_2\text{O}_4@\text{Ti}_3\text{C}_2$ MXene. **D)** $\text{S}_2\text{O}_8^{2-}$ binding to Ti sites on Ti_3C_2 MXene. **E)** Cyclic voltammograms of CoFe_2O_4 , Ti_3C_2 MXene and $\text{CoFe}_2\text{O}_4@\text{Ti}_3\text{C}_2$ MXene. **F)** Nyquist plots of CoFe_2O_4 , Ti_3C_2 MXene and $\text{CoFe}_2\text{O}_4@\text{Ti}_3\text{C}_2$ MXene.

the absence of Ti_3C_2 MXene, CoFe_2O_4 particles aggregated, limiting electron transfer and resulting in lower reactivity. The Nyquist diagram of EIS is shown in Fig. 6F. A linear portion was visible, and a semicircle appeared after magnifying the high-frequency data of EIS. This can be attributed to charge transfer and mass transfer resistance [51]. The radius of the semicircle represents the interface resistance of the electrode surface of the material [52], and $\text{CoFe}_2\text{O}_4@\text{Ti}_3\text{C}_2$ MXene possesses the smallest radius; thus, the charge transfer resistance decreased, which can not only speed up the electron transfer but also improve the catalytic activity of PS [53].

3.4. Transformation products and degradation pathways

The degradation products of OTA, AFB₁, GT and DON in the $\text{CoFe}_2\text{O}_4@\text{Ti}_3\text{C}_2$ MXene/PS system were determined to further explore the mechanisms of biotoxin transformation. Through high-performance liquid chromatography—mass spectrometry (HPLC—MS), a total of 20, 24, 11 and 14 degradation products were found for OTA, AFB₁, GT, and DON, respectively. The HPLC-MS/MS spectra are displayed in (Fig. S16–S84), and the corresponding chemical structure, retention time, m/z and toxic records of the degradation products are shown in Tables S8, S9, S10 and S11 for OTA, AFB₁, GT, and DON, respectively. Based on the

degradation product data and previous reports, the possible degradation pathways of OTA, AFB₁, GT and DON are shown in Fig. 7. Furthermore, the condensed Fukui function image (Fig. 7, in which an increased susceptibility for reaction with ROS is indicated by a more intense red color) based on DFT predicted the reaction active sites of biotoxin molecules, and specific values (f^0) are shown in Table S12. The condensed Fukui function can express the nucleophile and electrophilic properties of various atomic sites within the molecule [54]. The higher the function value of the atomic site, the stronger the electron-rich ability, so the easier it is to electrophilic reaction with ROS. Especially when different functional groups are present, it causes the electron arrangement between atoms to change, the images of condensed Fukui function calculation make it easier to visualize the electron-rich sites.

Multiple degradation pathways have been identified for OTA (Fig. 7A), and combining the results of the condensed Fukui function reveals the main degradation pathways. First, Cl28 was electrophilically attacked by $\text{SO}_4^{\bullet-}$ and $\bullet\text{OH}$ due to its high electron population. Then Cl28 was dechlorinated to generate P9, and decarboxylation and bond breakage generated P13 and P19 ($\text{OTA} \rightarrow \text{P9} \rightarrow \text{P10} \rightarrow \text{P13/P19}$). P9 can also generate P12, P16, P18 and P20 through bond breaking, hydrogenation, dehydroxylation, deamination and decarboxylation ($\text{OTA} \rightarrow \text{P9} \rightarrow \text{P3} \rightarrow \text{P12}$, $\text{OTA} \rightarrow \text{P9} \rightarrow \text{P16}$, $\text{OTA} \rightarrow \text{P9} \rightarrow \text{P3} \rightarrow \text{P18}$,

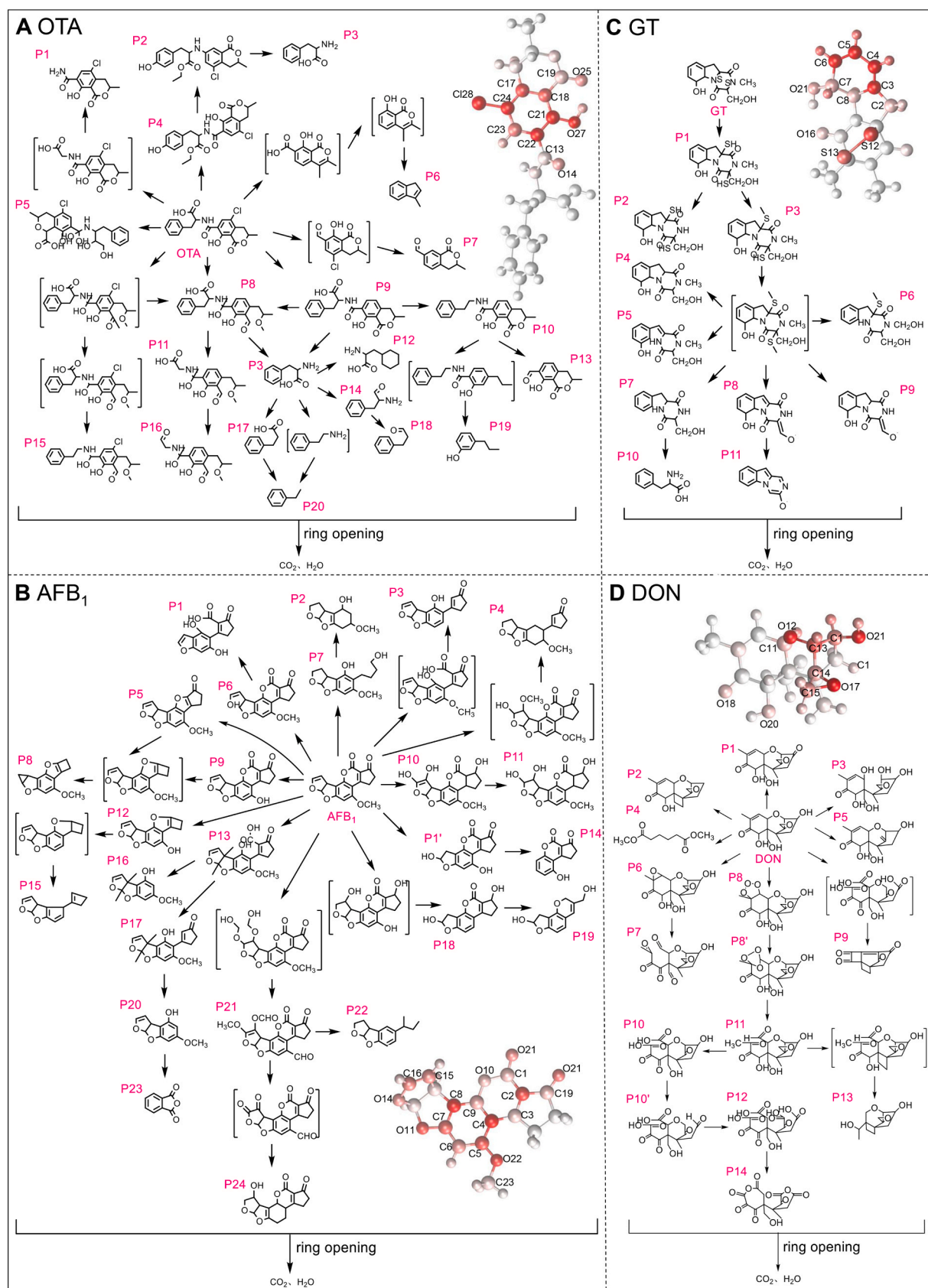


Fig. 7. The condensed Fukui function and degradation pathway. Potential degradation pathways of **A)** OTA, **B)** AFB₁, **C)** GT and **D)** DON in the CoFe₂O₄@Ti₃C₂ MXene/PS system. And the condensed Fukui function atom coloring diagram of OTA, AFB₁, GT and DON, calculated based on density functional theory (DFT). The redder the atom, the larger the condensed Fukui function.

OTA→P9→P3→P20). Second, C15 was also attacked by ROS, and P7 (OTA→P7) was generated through ring rupture, dechlorination and dehydroxylation. After the degradation intermediates undergo ring opening and oxidation to CO₂ and H₂O, small molecules may be produced that are too low in concentration or are quickly converted and not detected.

The transformation pathways of AFB₁ are displayed in Fig. 7B. AFB₁ also undergoes multiple degradation pathways, but based on the condensed Fukui function, the most likely scenario is that C15, C16, O10, O14 and O22 were attacked by SO₄^{•−}, •OH and O₂^{•−}. C15 and/or C16 and O22 were attacked by ROS, and P4, P11, P14, P19, P22 and P24 were generated with the following series of reactions: hydroxylation, hydrogenation, demethylation, decarboxylation ring opening, etc. (AFB₁→P4, AFB₁→P10→P11, AFB₁→P1'→P14, AFB₁→P18→P19, AFB₁→P21→P22/P24). In addition, O10 was likely attacked and converted into P2, P3, P16 and P23 by ring opening, bond breaking, hydrogenation, and hydroxyl substitution/dehydroxylation (AFB₁→P7→P2, AFB₁→P3, AFB₁→P13→P16, AFB₁→P13→P17→P20→P23). In addition, the O14 and O22 sites were attacked by SO₄^{•−} and •OH, and AFB₁ was converted to P1 through ring opening and demethylation (AFB₁→P6→P1).

The pathway of GT degradation is relatively simple (Fig. 7C). ROS attacks and breaks the S—S bond, and P2, P4, P5, P6, P9, P10 and P11 are produced through S—S bond breakage, demethylation, methyl substitution, desulfurization, dehydroxylation, ring opening and other reactions (GT→P1→P2, GT→P1→P3/P4/P5/P6/P9, GT→P1→P3→P7→P10, GT→P1→P3→P8→P11). These intermediates may be further oxidized and degraded into H₂O, CO₂, and some low molecular mass degradation products that could not be detected.

The pathways of DON transformation are displayed in Fig. 7D. The SO₄^{•−} attacks the O21 site to transform DON into oxidation product P1 (DON→P1), which exhibits a potential for dehydroxylation and cyclization to P2 (DON→P2). The O12 site was attacked by •OH, leading to ring opening and hydroxylation to P3 (DON→P3). O17 was attacked by SO₄^{•−} and O₂^{•−}, resulting in ring opening and deoxygenation to generate P5 (DON→P5). C13 and other C sites in DON were susceptible to attack by SO₄^{•−}, •OH and O₂^{•−}, resulting in ring-opening and oxidation to form P9 (DON→P9). In addition, the DON molecule may also be degraded by oxygen addition, ring opening, etc. However, according to the results of the condensed Fukui function, it is unlikely that these are the primary degradation pathways.

4. Discussion

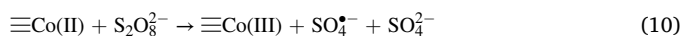
The characterization of the CoFe₂O₄@Ti₃C₂ MXene catalyst shows that layered Ti₃C₂ MXene was prepared. According to previous reports, MXenes have different properties than other supports, including functional group control, active material load, heteroatom doping structural design and defect engineering [55]. The layered Ti₃C₂ MXene prepared in this study has many advantages. First, MXene materials played a dual role, acting as a solid support and maximizing the utilization of catalytic active sites [25]. Second, compared with other non-metallic catalysts such as g-C₃N₄ and carbon nanotubes, Ti₃C₂ MXene enhanced the charge transfer kinetics between the MXene and the active component CoFe₂O₄ indirectly contributes to the catalytic activity [25]. Third, during the synthesis process, Ti₃C₂ MXene effectively prevented the accumulation and agglomeration of CoFe₂O₄, which in turn prepared the nanocatalyst on the surface of Ti₃C₂ MXenes and expanded its surface area, which was conducive to catalytic activity [56]. Fourth, Ti₃C₂ MXene has surface functional groups, which can enhance its hydrophilicity, redox activity, interaction with CoFe₂O₄ [57,58]. Fifth, due to the particularity of the preparation, transition metal vacancy defects would be formed on the surface of MXene, which has a certain effect on the catalysis of persulfate oxidizers [59]. Sixth, the possible existence of oxygen-containing functional groups such as -O at the end group of MXene will enhance its stability and oxidation resistance, and the internal Ti atom is protected by the -O group, which is conducive to its reuse [60].

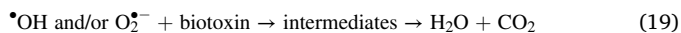
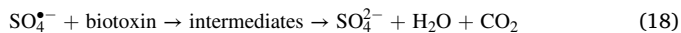
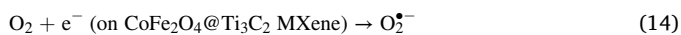
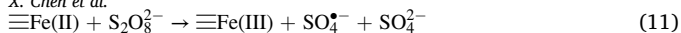
The CoFe₂O₄ particles were successfully supported by Ti₃C₂ MXene. The degradation of biotoxins shows that CoFe₂O₄@Ti₃C₂ MXene activates PS to effectively transform biotoxins. However, the components CoFe₂O₄ and Ti₃C₂ MXene also show a certain catalytic effect on PS. The catalytic activity of Ti₃C₂ MXene may be based on the vacancy defects, and the presence of Ti vacancies in Ti₃C₂ MXene were detected by AC-STEM in Fig. S13A. Chen et al. reported the Mo₂C MXene with vacancy defects can efficiently degrade bisphenol A [59]. In some carbon-based materials, it is easy to find the existence of defects, such as Ren et al. reported the defective carbon prepared from plastic waste showed excellent catalytic efficiency in PMS activation [61]. It also has been reported that Ti₃AlC₂ destroys part of the Ti-C bond during the corrosion process, resulting in a loss of Ti atoms and the formation of vacancy defects, which exhibit strong reducibility [62–64]. This is consistent with the pronounced signal peak of Ti₃C₂ MXene based on EPR analysis (Fig. S13B) and the g value of 2.004, which is characteristic of delocalized/free electrons caused by defects in the solid; in contrast, no signal was observed for Ti₃AlC₂. Additionally, the catalytic activity of CoFe₂O₄ and Ti₃C₂ MXene for PS may also be caused by the hydroxyl functional groups on the surface, because the oxygen-containing functional groups can improve the hydrophilicity of the material surface, thus strengthening the bonding of the catalyst with S₂O₈^{2−}, thereby improving the ability of transfer electrons to stimulate the production of ROS [39,65].

When CoFe₂O₄@Ti₃C₂ MXene is utilized, its ability to accelerate the decomposition of PS to generate ROS gradually decreases, especially for the removal of DON (Fig. 2B), which may be caused by Co and Fe ions leaching on the catalyst surface. As displayed in Fig. S14B, in the four degradation systems, leaching amounts measured for Co and Fe were 0.025–2.560 mg L^{−1} and 0.002–0.493 mg L^{−1}, respectively. The leaching of these ions is not conducive to the Co(II)/Co(III) and Fe(II)/Fe(III) cycles. The reduced degradation efficiency of OTA, AFB₁, GT, and DON in natural waters might be mainly due to the side reactions of inorganic anions and organic matter in natural waters with ROS, which compete with the biotoxins [66,67].

In general, HOMO and LUMO can predict the excitation properties and electron transport capabilities of molecules. The higher the energy level of the HOMO is, the stronger its ability to donate electrons, which is more conducive to electrophilic attacks. The HOMO-LUMO gap determines the reactivity of the organics, and it can be used to analyze the stability of the molecule and chances it will react. High HOMO and low LUMO energies in the LUMO-HOMO gaps can contribute to the electron transfer and addition reactions of π bonds in arenes and amides, respectively [68]. There is a correlation between the *K* values of the biotoxins studied and their HOMO-LUMO gap. The smaller the HOMO-LUMO gap is, the easier the electronic transition in the chemical reaction and the greater the chemical activity of the biotoxin molecules, resulting in attack by ROS and efficient decomposition.

The EPR results indicate that the removal of biotoxins in the CoFe₂O₄@Ti₃C₂ MXene/PS system was mainly a free radical process. A quantity of •OH and O₂^{•−} was produced in the CoFe₂O₄@Ti₃C₂ MXene/PS system, and CoFe₂O₄@Ti₃C₂ MXene exhibited a high degree of catalytic activation to PS. This result is also supported by the decomposition of PS. ≡Co(II) and ≡Fe(II) as active sites catalyzed PS (S₂O₈^{2−}) by electron transfer to produce SO₄^{•−} (Eqs. (10)–(11)) [34]. The modest signal of SO₄^{•−} was most likely due to it being quickly converted to •OH soon after it was generated, which occurred through a nucleophilic substitution reaction with OH[−] or H₂O (Eqs. (12)–(13)) [69]. And the free oxygen was reduced by a single electron on the catalyst surface to form O₂^{•−} (Eq. (14)) [27,70]. The coexistence of SO₄^{•−}, •OH and O₂^{•−} may interact to lead to the production of ¹O₂ (Eqs. (15)–(17)) [71]. The ROS (SO₄^{•−}, •OH and O₂^{•−}) can degrade biotoxins into intermediates, which eventually mineralize into H₂O and CO₂ (Eqs. (18)–(19)).



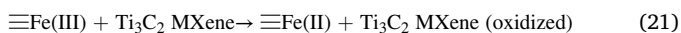


Based on the results of quenching experiment, the contribution of $\bullet\text{OH}$ for biotoxins degradation was much greater than that of other ROS. The contribution of $\bullet\text{OH}$ was about 78.27%-99.62%, $\text{SO}_4^{\bullet-}$ was about 0.06%-20.95%, and $\text{O}_2^{\bullet-}$ was about 0.09%-17.72%. In addition, p-BQ, as a typical scavenger of $\text{O}_2^{\bullet-}$, also has high reactivity with $\bullet\text{OH}$, the reaction rate constant is $\text{p-BQ}_{\text{O}_2^{\bullet-}} = 9.0 \times 10^8 - 1.0 \times 10^9 \text{ M}^{-1}\text{s}^{-1}$ and $\text{p-BQ}_{\bullet\text{OH}} = 1.2 \times 10^9 \text{ M}^{-1}\text{s}^{-1}$ [72,73]. Therefore, when considering the specific contribution of $\text{O}_2^{\bullet-}$ to biotoxin degradation, the contribution of $\bullet\text{OH}$ would be deducted. Based on the consumption of PS, the specific oxidation efficiency (SOE) of the $\text{CoFe}_2\text{O}_4/\text{Ti}_3\text{C}_2$ MXene/PS system can be calculated by Eq. (20) [69].

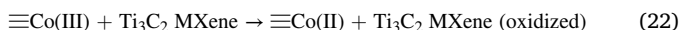
$$\text{SOE} = \frac{(\text{C}_{0,\text{biotoxin}} - \text{C}_{\text{t,biotoxin}})/\text{C}_{0,\text{biotoxin}}}{(\text{PS}_0 - \text{PS}_\text{t})/\text{PS}_0} \quad (20)$$

where the unit of C and PS are expressed based on mmol L^{-1} . The value of SOE of $\text{CoFe}_2\text{O}_4/\text{Ti}_3\text{C}_2$ MXene/PS system for the degradation of OTA, AFB₁, GT and DON were 1.51, 1.39, 1.27, 1.28, respectively. And compared with the PS-based system in literature, the $\text{CoFe}_2\text{O}_4/\text{Ti}_3\text{C}_2$ MXene/PS system has higher oxidation efficiency [74].

$\text{CoFe}_2\text{O}_4/\text{Ti}_3\text{C}_2$ MXene is a polycrystalline catalyst, and the content and valence of transition metal elements are very significant for the study of the whole catalytic mechanism of PS. After $\text{CoFe}_2\text{O}_4/\text{Ti}_3\text{C}_2$ MXene is used, the decrease in Co and Fe content may be attributed primarily to ion leaching due to corrosion, which is consistent with the result shown in Fig. S14. The $\text{S}_2\text{O}_8^{2-}$ adsorbed on $\text{CoFe}_2\text{O}_4/\text{Ti}_3\text{C}_2$ MXene and then the O-O bond broken to form $\text{SO}_4^{\bullet-}$ by accepting electrons from Co(II) and Fe(II) via Co-O and Fe-O covalent bonds (Eqs. (10) and (11)), leading to an increase in valence state. The change in the Fe valence state indicates the system exhibits reducing conditions. The exposed Ti atoms of Ti_3C_2 or Ti_2C MXene show strong reducibility, and these compounds have been reported to reduce U(VI) and Co(III) [62], so $\equiv\text{Fe(III)}$ may be reduced according to Eq. (21); in addition, the reduction in $\equiv\text{Ti(II)}$ content may also support this result.



After $\text{CoFe}_2\text{O}_4/\text{Ti}_3\text{C}_2$ MXene was used in four repeat cycles, the change in the chemical state of Co shows that $\equiv\text{Co(III)}$ was also reduced. The two possible reasons are as follows: (i) Ti, which exhibits a strong reducing ability in Ti_3C_2 MXene, contributes to the reduction in $\equiv\text{Co(III)}$ according to Eq. (22); or (ii) there is a difference in standard reduction potential between $\equiv\text{Fe(III)}/\equiv\text{Fe(II)}$ (0.77 V) and $\equiv\text{Co(III)}/\equiv\text{Co(II)}$ (1.84 V), similar to the interaction between $\equiv\text{Cu(III)}/\equiv\text{Cu(II)}$ (2.4 V) and $\equiv\text{Fe(III)}/\equiv\text{Fe(II)}$ [39,75]. Thus, it is suspected that $\equiv\text{Co(III)}$ can be reduced by the $\equiv\text{Fe(II)}$ present in the $\text{CoFe}_2\text{O}_4/\text{Ti}_3\text{C}_2$ MXene nanocomposite (Eq. (23)). The change in the chemical state of Fe shows that $\equiv\text{Fe(II)}$ was also used when $\equiv\text{Fe(III)}$ was reduced to $\equiv\text{Fe(II)}$. $\equiv\text{Fe(II)}$ may also activate PS (Eq. (11)) and participate in the $\equiv\text{Co(III)}/\equiv\text{Co(II)}$ (Eq. (23)) cycle.



The CV and EIS experiments confirmed that $\text{CoFe}_2\text{O}_4/\text{Ti}_3\text{C}_2$ MXene facilitated electron transfer and redox reactions and improved the reactivity. The negative adsorption energy between $\text{CoFe}_2\text{O}_4/\text{Ti}_3\text{C}_2$ MXene and PS indicates that PS was easily adsorbed onto $\text{CoFe}_2\text{O}_4/\text{Ti}_3\text{C}_2$ MXene. These aspects all demonstrated the advantages of $\text{CoFe}_2\text{O}_4/\text{Ti}_3\text{C}_2$ MXene in PS activation. Co and Fe act as activators in the multi-metallic catalyst $\text{CoFe}_2\text{O}_4/\text{Ti}_3\text{C}_2$ MXene, while Ti acts to enhance electron transfer between transition metals. Based on these results, the mechanism by which $\text{CoFe}_2\text{O}_4/\text{Ti}_3\text{C}_2$ MXene activates PS to degrade biotoxins was proposed, as shown in Fig. 8.

The current goal of detoxifying OTA is to degrade it into Ota ($\text{C}_{11}\text{H}_9\text{O}_5\text{Cl}$), which exhibits a toxicity 1000 times lower and a half-life 10 times shorter than that of OTA [76]. In the $\text{CoFe}_2\text{O}_4/\text{Ti}_3\text{C}_2$ MXene/PS/OTA system, the Ota was not detected, likely because it is unstable and quickly degraded. Additionally, the $\text{OTA} \rightarrow \text{P6/P7}$ pathway may involve Ota . The bifuran ring in AFB₁, especially the double bond in the furan ring, determines the toxicity of AFB₁, and the oxidized heterophenone determines the carcinogenicity of AFB₁ [77]. According to those results, $\text{SO}_4^{\bullet-}$, $\bullet\text{OH}$ and $\text{O}_2^{\bullet-}$ all act on the toxic sites of AFB₁ through multiple pathways, leading to their degradation and reduced toxicity. The toxicity of GT occurs due to its S—S bond, and in the $\text{CoFe}_2\text{O}_4/\text{Ti}_3\text{C}_2$ MXene/PS system, the first step involved ROS targeting the S—S bond, resulting in further degradation. Thus, $\text{CoFe}_2\text{O}_4/\text{Ti}_3\text{C}_2$ MXene effectively reduces the toxicity of GT. The toxicity of DON is mainly determined by the C=C bond, epoxy groups and the three -OH groups [78]. In the $\text{CoFe}_2\text{O}_4/\text{Ti}_3\text{C}_2$ MXene/PS system, most of the sites attacked by ROS are these toxic sites. Therefore, $\text{CoFe}_2\text{O}_4/\text{Ti}_3\text{C}_2$ MXene can effectively reduce the toxicity of DON in solution. In addition, it was found that the OTA degradation products P3, P9, P18 and P20; AFB₁ degradation products P10, P20 and P23; GT degradation product P10; and DON degradation product P4 had known toxicity data records (Table S8-S11), and those toxicity data from the sigma-aldrich website reagent safety data sheet (SDS). Compared to the parent molecules, these degradation products exhibit far less toxicity and do not cause harm to the environment and human body, indicating that the $\text{CoFe}_2\text{O}_4/\text{Ti}_3\text{C}_2$ MXene/PS system not only degraded the biotoxins but also effectively reduced their toxicity in the water matrix. Overall, these findings indicate that $\text{CoFe}_2\text{O}_4/\text{Ti}_3\text{C}_2$ MXene nanocomposite can be used as a potential catalyst for oxidizing a wide range of biotoxins that exhibit a wide range of applications in both environmental remediation and food safety.

5. Conclusion

In summary, a novel $\text{CoFe}_2\text{O}_4/\text{Ti}_3\text{C}_2$ MXene nanocomposite was successfully prepared by the hydrothermal synthesis method. Above findings indicate that this nanocomposite exhibited excellent PS catalytic performance, and the oxidation-based treatment constructed by $\text{CoFe}_2\text{O}_4/\text{Ti}_3\text{C}_2$ MXene and PS has broad-spectrum removal efficiency for a variety of biotoxins. $\text{CoFe}_2\text{O}_4/\text{Ti}_3\text{C}_2$ MXene shows a strong adsorption capacity, strong electron transfer ability and low charge transfer resistance for PS, and the Co and Fe sites activated PS through electron transfer and produced large amounts of ROS to degrade biotoxins. The possible degradation pathways of representative biotoxins OTA, AFB₁, GT and DON were proposed by evaluating the transformed products and based on condensed Fukui function calculations. $\text{CoFe}_2\text{O}_4/\text{Ti}_3\text{C}_2$ MXene has satisfactory repeatability, and the catalyst's own $\text{Co(III)}/\text{Co(II)}$ and $\text{Fe(III)}/\text{Fe(II)}$ cycles contribute significantly to its repeatability, which is not available in previously studied catalysts. Moreover, the oxidation system also maintains a high removal effect on biotoxins in actual natural water bodies. Although the development of MXene-based catalysts has made some progress in recent years, especially in the field of photocatalysis, the research of MXene as a persulfate activator for environmental applications is still in its infancy. This study proposed a new strategy for constructing a multifunctional MXene-based catalyst with high catalytic capacity, and provided an example

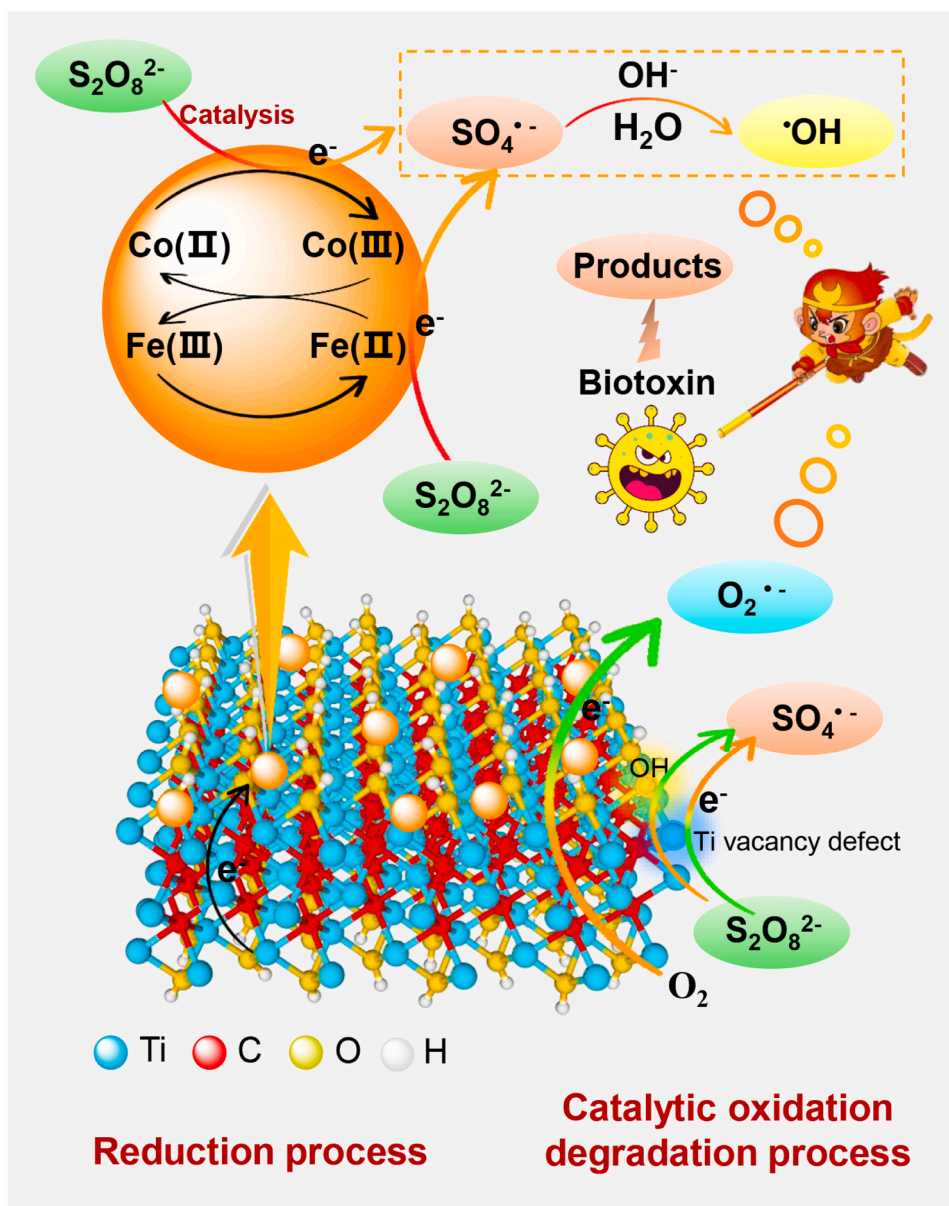


Fig. 8. Schematic illustration of the reaction mechanism for biotoxins removal by CoFe₂O₄@Ti₃C₂ MXene activated PS.

of broad-spectrum removal of multiple types of biotoxins by MXene-based SO₄^{•-}-AOPs technology. This work was more advanced than the common AOPs that only can remove a single type of pollutants, and provided a valuable reference for further harmless removal of mycotoxins and plant toxins from domestic sewage, industrial wastewater and medical wastewater. It also provided a novel approach for the development and application of MXene-based AOPs technology in environmental remediation and food safety.

Author Information

The authors declare no competing financial interest.

CRediT authorship contribution statement

Xuwen Chen: Writing – review & editing, Writing – original draft, Methodology, Investigation, Formal analysis, Data curation, Conceptualization. **J. Brett Sallach:** Writing – review & editing, Formal analysis, Data curation. **Wanting Ling:** Writing – review & editing, Methodology.

Xuqiang Zhao: Investigation, Formal analysis. **Thomas Borch:** Writing – review & editing. **Yanzheng Gao:** Writing – review & editing, Supervision, Resources, Project administration, Funding acquisition, Data curation.

Declaration of Competing Interest

The authors declare that they have no known competing financial interests or personal relationships that could have appeared to influence the work reported in this paper.

Data Availability

Data will be made available on request.

Acknowledgments

This work was financially supported by the National Science Fund for Distinguished Young Scholars (41925029), the National Natural Science

Foundation of China (22161132011, U22A20590, 42307031), and the Jiangsu Provincial Special Fund for S&T Innovation in Carbon Emission Peak and Neutrality (20220013), and the National Key Research and Development Program of China (2023YFE0110800), and China Postdoctoral Science Foundation (2023M731723), and Jiangsu Funding Program for Excellent Postdoctoral Talent (2023ZB478).

Appendix A. Supporting information

Supplementary data associated with this article can be found in the online version at doi:10.1016/j.apcatb.2024.123953.

References

- [1] J.W. Bennett, M. Klich, Mycotoxins, *Clin. Microbiol. Rev.* 16 (2003) 497–516.
- [2] A. Khataee, H. Sohrabi, O. Arbabzadeh, P. Khaaki, M.R. Majidi, Frontiers in conventional and nanomaterials based electrochemical sensing and biosensing approaches for Ochratoxin A analysis in foodstuffs: A review, *Food Chem. Toxicol.* 149 (2021) 112030.
- [3] G.A. Pena, C.M. Pereyra, M.R. Armando, S.M. Chiacchiera, C.E. Magnoli, J. L. Orlando, A.M. Dalcero, C.A.R. Rosa, L.R. Cavaglieri, *Aspergillus fumigatus* toxicity and gliotoxin levels in feedstuff for domestic animals and pets in Argentina, *Lett. Appl. Microbiol.* 50 (2010) 77–81.
- [4] S. Wu, F. Wang, Q. Li, J. Wang, Y. Zhou, N. Duan, S. Niazi, Z. Wang, Photocatalysis and degradation products identification of deoxynivalenol in wheat using upconversion nanoparticles@TiO₂ composite, *Food Chem.* 323 (2020) 126823.
- [5] L. Winnie-Pui-Pui, M.R. Sabran, Mycotoxin: Its Impact on Gut Health and Microbiota, *Front. Cell. Infect.* 8 (2018) 60.
- [6] S. Quintela, M.C. Villarán, I. López de Armentia, E. Elejalde, Ochratoxin A removal in wine: A review, *Food Control* 30 (2013) 439–445.
- [7] R. Karami-Osboo, M. Mirabolfathy, R. Kamran, M. Shetab-Boushehri, S. Sarkari, Aflatoxin B1 in maize harvested over 3 years in Iran, *Food Control* 23 (2012) 271–274.
- [8] Y. Gong, A. Houns, S. Egal, P.C. Turner, A.E. Sutcliffe, A.J. Hall, K. Cardwell, C. P. Wild, Postweaning exposure to aflatoxin results in impaired child growth: a longitudinal study in Benin, West Afr., *Environ. Health Persp.* 112 (2004) 1334–1338.
- [9] A. van den Berg, H.G. Craighead, P. Yang, From microfluidic applications to nanofluidic phenomena, *Chem. Soc. Rev.* 39 (2010) 899–900.
- [10] F. Malir, V. Ostry, A. Pfohl-Leszkowicz, J. Malir, J. Toman, Ochratoxin A: 50 Years of Research, *Toxins* 8 (2016) 191.
- [11] M.R. Rezaie, N. Zareie, Impact of granite irradiation on aflatoxin reduction in pistachio, *Toxicon* 199 (2021) 7–11.
- [12] B.A. Young, E.A. Burdman, R.J. Johnson, T. Andoh, W.M. Bennett, W.G. Couser, C.E. Alpers, Cyclosporine A induced arteriopathy in a rat model of chronic cyclosporine nephropathy, *Kidney Int* 48 (1995) 431–438.
- [13] M. Kroll, F. Arenzana-Seisdedos, F. Bachelier, D. Thomas, B. Friguet, M. Conconi, The secondary fungal metabolite gliotoxin targets proteolytic activities of the proteasome, *Chem. Biol.* 6 (1999) 689–698.
- [14] J. Pestka, A. Smolinski, Deoxynivalenol: Toxicology and Potential Effects on Humans, *J. Toxicol. env. Heal. B.* 8 (2005) 39–69.
- [15] H. Zheng, J. Bao, Y. Huang, L. Xiang, B. Faheem, J. Ren, M.N. Du, D.D. Nadagouda, Dionysiou, Efficient degradation of atrazine with porous sulfurized Fe₂O₃ as catalyst for peroxymonosulfate activation, *Appl. Catal. B: Environ.* 259 (2019) 118056.
- [16] W. Li, S. Patton, J.M. Gleason, S.P. Mezyk, K.P. Ishida, H. Liu, UV Photolysis of Chloramine and persulfate for 1,4-dioxane removal in reverse-osmosis permeate for potable water reuse, *Environ. Sci. Technol.* 52 (2018) 6417–6425.
- [17] J. Wang, J. Yu, Q. Fu, H. Yang, Q. Tong, Z. Hao, G. Ouyang, Unprecedented Nonphotomediated Hole (h⁺) oxidation system constructed from defective carbon nanotubes and superoxides, *ACS Cent. Sci.* 7 (2021) 355–364.
- [18] J. Moreno-Andrés, G. Farinango, L. Romero-Martínez, A. Acevedo-Merino, E. Nebot, Application of persulfate salts for enhancing UV disinfection in marine waters, *Water Res* 163 (2019) 114866.
- [19] Y. Yang, P. Zhang, K. Hu, P. Zhou, Y. Wang, A.H. Asif, X. Duan, H. Sun, S. Wang, Crystallinity and valence states of manganese oxides in Fenton-like polymerization of phenolic pollutants for carbon recycling against degradation, *Appl. Catal. B: Environ.* 315 (2022) 121593.
- [20] Y. Yao, H. Hu, H. Yin, Z. Ma, Z. Tao, Y. Qiu, S. Wang, Pyrite-embedded porous carbon nanocatalysts assembled in polyvinylidene difluoride membrane for organic pollutant oxidation, *J. Colloid Interf. Sci.* 608 (2022) 2942–2954.
- [21] K. He, W. Li, L. Tang, L. Chen, G. Wang, Q. Liu, X. Xin, C. Yang, Z. Wang, S. Lv, D. Xing, Insight into the design of a Ti₃C₂ MXene/Ti₄O₇ composite ceramic membrane boosts the electrocatalytic activity for 1,4-dioxane electro-oxidation, *Appl. Catal. B: Environ.* 338 (2023) 123077.
- [22] R. Pelalak, A. Hassani, Z. Heidari, M. Zhou, State-of-the-art recent applications of layered double hydroxides (LDHs) material in Fenton-based oxidation processes for water and wastewater treatment, *Chem. Eng. J.* 474 (2023) 145511.
- [23] B. Zhang, Y. Wang, Z. Wang, G. Tan, T. Liu, S. Feng, Y. Tan, W. Liu, Q. Yang, Y. Liu, A. Xia, H. Ren, Y. Wu, Surface plasmon resonance effects of Ti₃C₂ MXene for degradation of antibiotics under full spectrum, *Appl. Catal. B: Environ.* 339 (2023) 123132.
- [24] Y. Gogotsi, B. Anasori, The Rise of MXenes, *ACS Nano* 13 (2019) 8491–8494.
- [25] P. Eghbali, A. Hassani, S. Wacławek, K.-Y. Andrew Lin, Z. Sayyar, F. Ghanbari, Recent advances in design and engineering of MXene-based catalysts for photocatalysis and persulfate-based advanced oxidation processes: A state-of-the-art review, *Chem. Eng. J.* 480 (2024) 147920.
- [26] M. Ghidui, M.R. Lukatskaya, M.Q. Zhao, Y. Gogotsi, M.W. Barsoum, Conductive two-dimensional titanium carbide ‘clay’ with high volumetric capacitance, *Nature* 516 (2014) 78–81.
- [27] B. Li, S. Liu, C. Lai, G. Zeng, M. Zhang, M. Zhou, D. Huang, L. Qin, X. Liu, Z. Li, N. An, F. Xu, H. Yi, Y. Zhang, L. Chen, Unravelling the interfacial charge migration pathway at atomic level in 2D/2D interfacial Schottky heterojunction for visible-light-driven molecular oxygen activation, *Appl. Catal. B: Environ.* 266 (2020) 118650.
- [28] M. Naguib, V.N. Mochalin, M.W. Barsoum, Y. Gogotsi, 25th Anniversary Article: MXenes: A New Family of Two-Dimensional Materials, *Adv. Mater.* 26 (2014) 992–1005.
- [29] Z. Ai, Y. Shao, B. Chang, B. Huang, Y. Wu, X. Hao, Effective orientation control of photogenerated carrier separation via rational design of a Ti₃C₂(TiO₂)@CdS/MoS₂ photocatalytic system, *Appl. Catal. B: Environ.* 242 (2019) 202–208.
- [30] Q. Wang, Y. Mei, R. Zhou, S. Komarneni, J. Ma, Persulfate activation of CuS@Ti₃C₂-based MXene with Bi-active centers toward Orange II removal under visible light, *Colloid Surf. A* 648 (2022) 129315.
- [31] Y. Cao, Y. Fang, X. Lei, B. Tan, X. Hu, B. Liu, Q. Chen, Fabrication of novel CuFe₂O₄/MXene hierarchical heterostructures for enhanced photocatalytic degradation of sulfonamides under visible light, *J. Hazard. Mater.* 387 (2020) 122021.
- [32] F. Yu, F. Zhu, H. Zhang, S. Komarneni, J. Ma, Efficient activation of K₂S₂O₈ by MoS₂-ZnFe₂O₄ composite for the rapid degradation of tetracycline, *Mater. Lett.* 318 (2022) 132204.
- [33] B. Zhu, H. Cheng, J. Ma, Y. Kong, S. Komarneni, Efficient degradation of rhodamine B by magnetically separable ZnS–ZnFe₂O₄ composite with the synergistic effect from persulfate, *Chemosphere* 237 (2019) 124547.
- [34] L. Wu, Q. Zhang, J. Hong, Z. Dong, J. Wang, Degradation of bisphenol A by persulfate activation via oxygen vacancy-rich CoFe₂O_{4-x}, *Chemosphere* 221 (2019) 412–422.
- [35] C. Tan, N. Gao, D. Fu, J. Deng, L. Deng, Efficient degradation of paracetamol with nanoscaled magnetic CoFe₂O₄ and MnFe₂O₄ as a heterogeneous catalyst of peroxymonosulfate, *Sep. Purif. Technol.* 175 (2017) 47–57.
- [36] K. Faungnawakij, N. Viriya-empikol, Catalytic behavior toward oxidative steam reforming of dimethyl ether over CuFe₂O₄-Al₂O₃ composite catalysts, *Appl. Catal. A: Gen.* 382 (2010) 21–27.
- [37] J. Lee, U. von Gunten, J.H. Kim, Persulfate-Based Advanced Oxidation: Critical Assessment of Opportunities and Roadblocks, *Environ. Sci. Technol.* 54 (2020) 3064–3081.
- [38] C. Lu, L. Yang, B. Yan, L. Sun, P. Zhang, W. Zhang, Z. Sun, Nitrogen-Doped Ti₃C₂ MXene: Mechanism Investigation and Electrochemical Analysis, *Adv. Funct. Mater.* 30 (2020) 2000852.
- [39] X. Dong, B. Ren, Z. Sun, C. Li, X. Zhang, M. Kong, S. Zheng, D.D. Dionysiou, Monodispersed CuFe₂O₄ nanoparticles anchored on natural kaolinite as highly efficient peroxymonosulfate catalyst for bisphenol A degradation, *Appl. Catal. B: Environ.* 253 (2019) 206–217.
- [40] M. Naguib, M. Kurtoglu, V. Presser, J. Lu, J. Niu, H. Min, L. Hultman, Y. Gogotsi, M.W. Barsoum, Two-dimensional nanocrystals produced by exfoliation of Ti₃AlC₂, *Adv. Mater.* 23 (2011) 4248–4253.
- [41] G. Kresse, J. Furthmüller, Efficiency of ab-initio total energy calculations for metals and semiconductors using a plane-wave basis set, *Com. Mater. Sci.* 6 (1996) 15–50.
- [42] G. Kresse, J. Furthmüller, Efficient iterative schemes for ab initio total-energy calculations using a plane-wave basis set, *Phys. Rev. B* 54 (1996) 11169–11186.
- [43] E. M. Generalized gradient approximation made simple, *Phys. Rev. Lett.* 77 (1996) 3865.
- [44] T. Lu, F. Chen, Multiwfn: A multifunctional wavefunction analyzer, *J. Comput. Chem.* 33 (2012) 580–592.
- [45] Y. Yang, Z. Zeng, G. Zeng, D. Huang, R. Xiao, C. Zhang, C. Zhou, W. Xiong, W. Wang, M. Cheng, W. Xue, H. Guo, X. Tang, D. He, Ti₃C₂ MXene/porous g-C₃N₄ interfacial Schottky junction for boosting spatial charge separation in photocatalytic H₂O₂ production, *Appl. Catal. B: Environ.* 258 (2019) 117956.
- [46] F. Hu, W. Luo, C. Liu, H. Dai, X. Xu, Q. Yue, L. Xu, G. Xu, Y. Jian, X. Peng, Fabrication of graphitic carbon nitride functionalized P-CoFe₂O₄ for the removal of tetracycline under visible light: Optimization, degradation pathways and mechanism evaluation, *Chemosphere* 274 (2021) 129783.
- [47] M. Wang, Y. Cui, H. Cao, P. Wei, C. Chen, X. Li, J. Xu, G. Sheng, Activating peroxydisulfate with Co₃O₄/NiCo₂O₄ double-shelled nanocages to selectively degrade bisphenol A – a nonradical oxidation process, *Appl. Catal. B: Environ.* 282 (2021) 119585.
- [48] S. Esplugas, J. Giménez, S. Contreras, E. Pascual, M. Rodríguez, Comparison of different advanced oxidation processes for phenol degradation, *Water Res* 36 (2002) 1034–1042.
- [49] Q. Ji, X. Cheng, Y. Wu, W. Xiang, H. He, Z. Xu, C. Xu, C. Qi, S. Li, L. Zhang, S. Yang, Visible light absorption by perylene diimide for synergistic persulfate activation towards efficient photodegradation of bisphenol A, *Appl. Catal. B: Environ.* 282 (2021) 119579.
- [50] P. Chen, L. Blaney, G. Cagnetta, J. Huang, B. Wang, Y. Wang, S. Deng, G. Yu, Degradation of Ofloxacin by Perylene Diimide Supramolecular Nanofiber Sunlight-Driven Photocatalysis, *Environ. Sci. Technol.* 53 (2019) 1564–1575.

- [51] P. Wang, S. Zhan, H. Wang, Y. Xia, Q. Hou, Q. Zhou, Y. Li, R.R. Kumar, Cobalt phosphide nanowires as efficient co-catalyst for photocatalytic hydrogen evolution over $\text{Zn}_{0.5}\text{Cd}_{0.5}\text{S}$, *Appl. Catal. B: Environ.* 230 (2018) 210–219.
- [52] W. Wang, Y. Liu, Y. Yue, H. Wang, G. Cheng, C. Gao, C. Chen, Y. Ai, Z. Chen, X. Wang, The Confined Interlayer Growth of Ultrathin Two-Dimensional Fe_3O_4 Nanosheets with Enriched Oxygen Vacancies for Peroxymonosulfate Activation, *ACS Catal.* 11 (2021) 11256–11265.
- [53] C. Zhu, S. Zhao, Z. Fan, H. Wu, F. Liu, Z. Chen, A. Li, Confinement of CoP Nanoparticles in Nitrogen-Doped Yolk-Shell Porous Carbon Polyhedron for Ultrafast Catalytic Oxidation, *Adv. Funct. Mater.* 30 (2020) 2003947.
- [54] J. Cao, Q. Ren, F. Chen, T. Lu, Comparative study on the methods for predicting the reactive site of nucleophilic reaction, *Sci. China Chem.* 58 (2015) 1845–1852.
- [55] J. Qiao, L. Kong, S. Xu, K. Lin, W. He, M. Ni, Q. Ruan, P. Zhang, Y. Liu, W. Zhang, L. Pan, Z. Sun, Research progress of MXene-based catalysts for electrochemical water-splitting and metal-air batteries, *Energy Storage Mater.* 43 (2021) 509–530.
- [56] K. Zhang, D. Li, H. Cao, Q. Zhu, C. Trapalis, P. Zhu, X. Gao, C. Wang, Insights into different dimensional MXenes for photocatalysis, *Chem. Eng. J.* 424 (2021) 130340.
- [57] X. Feng, Z. Yu, Y. Sun, R. Long, M. Shan, X. Li, Y. Liu, J. Liu, Review MXenes as a new type of nanomaterial for environmental applications in the photocatalytic degradation of water pollutants, *Ceram. Int.* 47 (2021) 7321–7343.
- [58] C. Prasad, X. Yang, Q. Liu, H. Tang, A. Rammohan, S. Zulfiqar, G.V. Zyryanov, S. Shah, Recent advances in MXenes supported semiconductors based photocatalysts: Properties, synthesis and photocatalytic applications, *J. Ind. Eng. Chem.* 85 (2020) 1–33.
- [59] X. Chen, F.O. Gudda, X. Hu, M.G. Waigi, Y. Gao, Degradation of bisphenol A in an oxidation system constructed from Mo_2C MXene and peroxymonosulfate, *npj Clean. Water* 5 (2022) 66.
- [60] B.R. Anne, J. Kundu, M.K. Kabiraz, J. Kim, D. Cho, S.I. Choi, A Review on MXene as Promising Support Materials for Oxygen Evolution Reaction Catalysts, *Adv. Funct. Mater.* 33 (2023) 2306100.
- [61] S. Ren, X. Xu, Z.S. Zhu, Y. Yang, W. Tian, K. Hu, S. Zhong, J. Yi, X. Duan, S. Wang, Catalytic transformation of microplastics to functional carbon for catalytic peroxymonosulfate activation: Conversion mechanism and defect of scavenging, *Appl. Catal. B: Environ.* 342 (2024) 123410.
- [62] H. Song, R. Du, Y. Wang, D. Zu, R. Zhou, Y. Cai, F. Wang, Z. Li, Y. Shen, C. Li, Anchoring single atom cobalt on two-dimensional MXene for activation of peroxymonosulfate, *Appl. Catal. B: Environ.* 286 (2021) 119898.
- [63] D. Zhao, Z. Chen, W. Yang, S. Liu, X. Zhang, Y. Yu, W.-C. Cheong, L. Zheng, F. Ren, G. Ying, X. Cao, D. Wang, Q. Peng, G. Wang, C. Chen, MXene (Ti_3C_2) Vacancy-Confining Single-Atom Catalyst for Efficient Functionalization of CO_2 , *J. Am. Chem. Soc.* 141 (2019) 4086–4093.
- [64] X. Tang, D. Zhou, P. Li, X. Guo, B. Sun, H. Liu, K. Yan, Y. Gogotsi, G. Wang, MXene-Based Dendrite-Free Potassium Metal Batteries, *Adv. Mater.* 32 (2020) 1906739.
- [65] Y. Liu, J. Luo, L. Tang, C. Feng, J. Wang, Y. Deng, H. Liu, J. Yu, H. Feng, J. Wang, Origin of the Enhanced Reusability and Electron Transfer of the Carbon-Coated Mn_3O_4 Nanocube for Persulfate Activation, *ACS Catal.* 10 (2020) 14857–14870.
- [66] J. Guo, Q. Gao, S. Yang, F. Zheng, B. Du, S. Wen, D. Wang, Degradation of pyrene in contaminated water and soil by Fe^{2+} -activated persulfate oxidation: Performance, kinetics, and background electrolytes (Cl^- , HCO_3^- and humic acid) effects, *Process Saf. Environ.* 146 (2021) 686–693.
- [67] X. Zhou, A. Jawad, M. Luo, C. Luo, T. Zhang, H. Wang, J. Wang, S. Wang, Z. Chen, Z. Chen, Regulating activation pathway of Cu/persulfate through the incorporation of unreducible metal oxides: Pivotal role of surface oxygen vacancies, *Appl. Catal. B: Environ.* 286 (2021) 119914.
- [68] R. Xiao, T. Ye, Z. Wei, S. Luo, Z. Yang, R. Spinney, Quantitative structure-activity relationship (qsar) for the oxidation of trace organic contaminants by Sulfate Radical, *Environ. Sci. Technol.* 49 (2015) 13394–13402.
- [69] Q. Ma, L.C. Nengzi, X. Zhang, Z. Zhao, X. Cheng, Enhanced activation of persulfate by $\text{AC@CoFe}_2\text{O}_4$ nanocomposites for effective removal of lomefloxacin, *Sep. Purif. Technol.* 233 (2020) 115978.
- [70] D.L. Ball, J.O. Edwards, The Kinetics and Mechanism of the Decomposition of Caro's Acid. I, *J. Am. Chem. Soc.* 78 (1956) 1125–1129.
- [71] W. Huang, S. Xiao, H. Zhong, M. Yan, X. Yang, Activation of persulfates by carbonaceous materials: A review, *Chem. Eng. J.* 418 (2021) 129297.
- [72] Z. Xu, Y. Wu, X. Wang, Q. Ji, T. Li, H. He, H. Song, S. Yang, S. Li, S. Yan, L. Zhang, Z. Zou, Identifying the role of oxygen vacancy on cobalt-based perovskites towards peroxymonosulfate activation for efficient iohexol degradation, *Appl. Catal. B: Environ.* 319 (2022) 121901.
- [73] X. Yang, P. Wu, W. Chu, G. Wei, Peroxymonosulfate/ LaCoO_3 system for tetracycline degradation: Performance and effects of co-existing inorganic anions and natural organic matter, *J. Water Process Eng.* 43 (2021) 102231.
- [74] X. Xu, S. Zong, W. Chen, D. Liu, Comparative study of Bisphenol A degradation via heterogeneously catalyzed H_2O_2 and persulfate: Reactivity, products, stability and mechanism, *Chem. Eng. J.* 369 (2019) 470–479.
- [75] H. Xu, D. Wang, J. Ma, T. Zhang, X. Lu, Z. Chen, A superior active and stable spinel sulfide for catalytic peroxymonosulfate oxidation of bisphenol S, *Appl. Catal. B: Environ.* 238 (2018) 557–567.
- [76] S. Li, R.R. Marquardt, A.A. Frohlich, T.G. Vitti, G. Crow, Pharmacokinetics of Ochratoxin A and Its Metabolites in Rats, *Toxicol. Appl. Pharm.* 145 (1997) 82–90.
- [77] H. Yazdanpanah, T. Mohammadi, G. Abouhossain, A.M. Cheraghali, Effect of roasting on degradation of Aflatoxins in contaminated pistachio nuts, *Food Chem. Toxicol.* 43 (2005) 1135–1139.
- [78] R. B. A, Rapid colorimetric bioassay for screening of Fusarium mycotoxins, *Nat. toxins* (5) (1993).